ministerie van verkeer en waterstaat

koninklijk nederlands meteorologisch instituut

The parameterization of vertical turbulent mixing processes in a General Circulation Model of the Tropical Pacific

G.Janssen

Scientific reports; WR-92-03
Wetenschappelijke rapporten; WR-92-03

De Bilt, 1992

De Bilt 1992

publicationnumber: Scientific reports = wetenschappelijke rapporten; WR 92-03

p.o. box 201
3730 AE De Bilt
Wilhelminalaan 10
tel.+31 30 206 911
telex 470 96

UDC: 551.465.45
551.526.63
(265)

ISSN: 0169-1651

ISBN: 90-369-2022-1

Abstract

General circulation models (GCM's) of the equatorial Pacific have some common problems. Equatorial sea surface temperatures are too low and also the characteristic equatorial thermocline structure (rising isotherms in the east and a warm pool in the west) is not simulated very well. Therefore we investigated the effect of turbulent surface mixing on these problems.

We find that the inclusion of a surface mixed layer can have a strong effect on both the temperature and the velocity structure of the modelled equatorial Pacific. The modelled SST's are in better agreement with observational data and a deep warm pool in the western Pacific can develop. We conclude that surface mixing in a coarse resolution GCM of the equatorial Pacific improves its performance.

Voorwoord

Dit rapport beschrijft een onderzoek dat tot stand is gekomen bij het KNMI in de Bilt. Het onderzoek is verricht in het kader van mijn afstudeerwerk aan de faculteit der Technische Natuurkunde van de Technische Universiteit Delft. Binnen de sectie Warmtetransport van de vakgroep Transportverschijnselen bestond de mogelijkheid het afstudeerwerk onder toezicht van prof. dr. J. Wieringa te verrichten op het KNMI.

Van 1 maart 1991 tot begin mei 1992 heb ik met veel plezier gewerkt op de afdeling Oceanografisch Onderzoek van het KNMI. Ik heb daar de invloed van de parametrisatie van verticale turbulente mengprocessen op het gedrag van een numeriek oceaanmodel onderzocht. Dit alles onder de zeer motiverende en inspirerende begeleiding van dr. Arie Kattenberg. Met hem wil ik ook Marc Allaart in het bijzonder bedanken, de modelbouwer, die steeds klaar stond om mij uit een computertechnisch moeras te trekken.

G. Janssen, 6 Mei, 1992.

The parameterization of vertical turbulent mixing processes in a General Circulation Model of the Tropical Pacific

G. Janssen

Contents

Symbols

b	buoyancy acceleration	ms^{-2}
B	buoyancy flux	$kgm^{-1}s^{-3}$
c	specific heat	m^2s^{-1}
C_d	drag coefficient	-
e	turbulence kinetic energy	m^2s^{-2}
e_a	water vapor pressure	-
E	evaporation rate	$kgm^{-2}s^{-1}$
f	Coriolis parameter	s^{-1}
g	gravitational acceleration	ms^{-2}
h_{ml}	ocean mixed layer depth	m
h_{obl}	ocean boundary layer depth	m
K_M	eddy viscosity	m^2s^{-1}
K_S	eddy salt diffusivity	m^2s^{-1}
K_T	eddy heat diffusivity	m^2s^{-1}
L	Obukhov length (m)	m
L_V	Latent heat of evaporation	Jkg^{-1}
n_c	cloud cover fraction	-
p	pressure	Nm^{-2}
P	precipitation rate	$kgm^{-2}s^{-1}$
q	specific humidity	-
Q	heat flux	Wm^{-2}
Ri	gradient Richardson number	-
S	salinity	permille
SST	sea surface temperature	°C
t	time	s
T	temperature	K
u_i	velocity vector	ms^{-1}
u_*	friction velocity	ms^{-1}
x_i	position vector	m
α	coefficient of thermal expansion	K^{-1}
α_S	surface albedo	-
β	coefficient of haline contraction	$permille^{-1}$
ϵ_{ijk}	alternating unit tensor	-
κ_S	salt diffusivity	m^2s^{-1}
κ_T	heat diffusivity	m^2s^1
μ	dynamic viscosity	$kgm^{-1}s^{-1}$
ν	kinematic viscosity	m^2s^{-1}
θ	potential temperature	K
ρ	density	kgm^{-3}
τ	shear stress	$kgm^{-1}s^{-2}$
Ω_i	angular velocity, earth rotation	s^{-1}

1 Introduction

1.1 The role of the upper ocean in the global climate

Oceans cover the greater part of the earth. About two-fifth of the total solar energy intercepted by our planet is absorbed by the oceans and one-tenth by the continents. The remainder is reflected and diffracted back into the universe or absorbed by the atmosphere (Fig. 1.1). (Two-thirds of the downward longwave radiation from the atmosphere is also absorbed by the ocean). The heat capacity of the ocean is about 1000 times that of the atmosphere so it can store much more heat than is needed to alter atmospheric balances. Not all of this heat is readily available because the ocean interior, where most of the heat capacity resides, is more or less isolated from the top layer of the ocean.

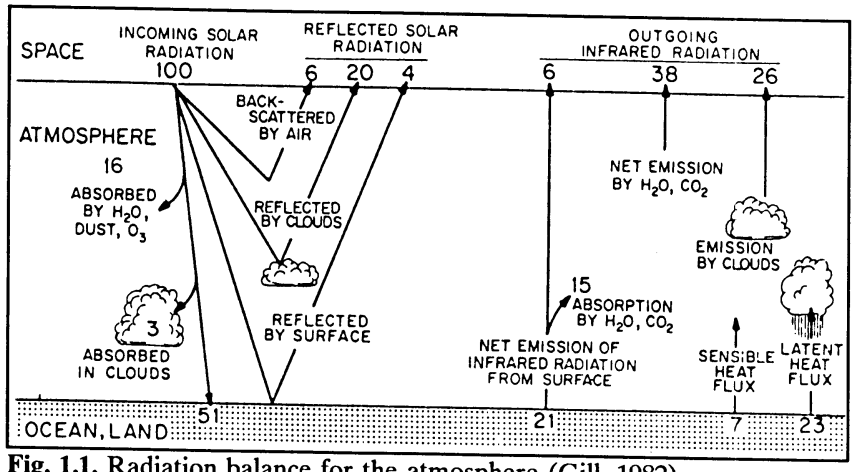

Fig. 1.1. Radiation balance for the atmosphere (Gill, 1982).

The incoming solar energy is not distributed evenly over the earth surface (Fig. 1.2). In the tropics more energy is received each year from the sun than is released to the atmosphere. The surplus is stored and transported by ocean currents to the mid-latitudes, where it is given off to the atmosphere.

So the ocean is not only storing heat but also transports it. This heat transport is basically lateral (i.e. parallel to the earth surface). The vertical oceanic heat transport, which takes place on smaller length and time scales, is of importance too. The vertical distribution of the energy received by the ocean surface is related to the existence of a turbulent ocean boundary layer (OBL). Such a layer is generated by mechanisms like shear flow instabilities, wave breaking and convection

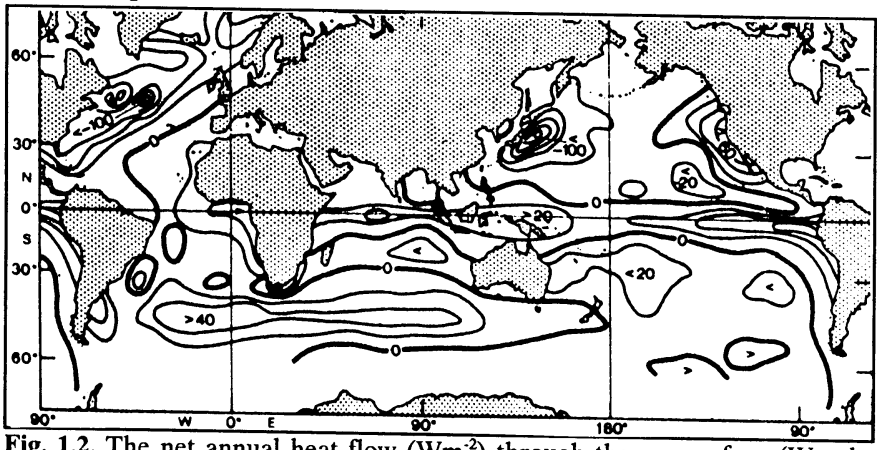

Fig. 1.2. The net annual heat flow (Wm^{-2}) through the sea surface (Woods, 1985).

driven by buoyancy loss (see section 2.1). The thickness of this layer varies and is typically between 20 m in warm, wind-deficient areas and 1000 m in cold windy regions.

One of the properties of a turbulent flow is its great capability of mixing. Due to this mixing the energy received by the ocean surface is distributed vertically over the depth of the ocean boundary layer. Large scale currents then transport it laterally over thousands of kilometres. So the upper turbulent ocean layer plays an important role in the storage of solar energy.

To make further improvements in climate modelling it is necessary to concentrate on two turbulent layers, i.e. the atmospheric boundary layer and the ocean boundary layer, which constitute the connection between the ocean and the atmosphere. If we wish to couple ocean and atmosphere in our simulations we need good models of these turbulent layers.

However, both the atmospheric and the ocean boundary layer are difficult environments in which to measure turbulent quantities. Much more effort has been directed to the atmospheric boundary layer. This is mainly because of the fact that we live in it. Consequently the atmospheric boundary layer is much better understood than its oceanic counterpart. In expectation of better measurement tools and techniques we should, however, keep on trying to solve the theoretical problems. After all it is clear that the ocean mixed layer plays a crucial role in the dynamics of the ocean atmosphere system. Woods summarizes: 'If air-sea interaction is the Achilles' heel of climate, then the upper ocean is the Achilles of climate prediction,'

For climate simulations a boundary layer model must be robust and accurate. It must permit calculation of the sea surface temperature to within 10% of the annual range, and the mixed layer depth to significantly better than 10% of the mean monthly value (Woods, 1985).

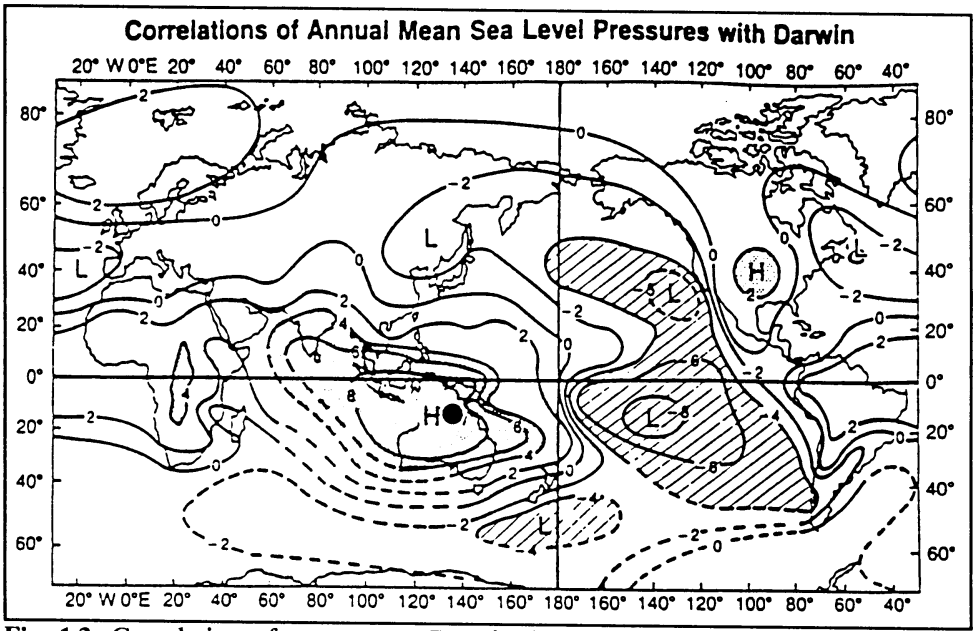

Fig. 1.3. Correlation of pressure at Darwin (Australia) with that at other stations around the world (Anderson and Willebrand, 1992).

Note the difference between the turbulent boundary layer and the mixed layer. The mixed layer is that part of the upper ocean where temperature and salinity are

distributed quasi-homogeneously with depth. The turbulent boundary layer is that part of the upper ocean that contains turbulence generated by air sea interaction processes (Müller and Garwood, 1988). Without having reached the limits of predictability, the present state of ocean boundary layer modelling doesn't meet the above mentioned specifications. A good prescription of how to parameterize the various physical processes controlling the structure of the turbulent layer does not yet exist.

In this investigation we have been studying the role of various mixing parameterizations in an Ocean General Circulation Model (OGCM) of the Equatorial Pacific. The purpose was to investigate how mixing processes affect the dynamics of such a model.

1.2 The El Niño southern oscillation (ENSO)

An interesting example of strong ocean atmosphere interaction is the so-called El Niño Southern Oscillation (ENSO). It is regarded as an irregular interannual oscillation of the coupled ocean/atmosphere system. When the pressure is high over the Pacific ocean, it tends to be low over the Indian Ocean from Africa to Australia, and vice versa (Fig. 1.3). This irregular fluctuation is called the Southern Oscillation and is an atmospheric response to an alternation of two states of the Equatorial Pacific: one state, which is both characterized by relatively cold sea surface temperatures (SST's) in the eastern Pacific, combined with a "pool" of warm water in the western Pacific (Fig. 1.4); and a state characterized by relatively warm SST's in the eastern Pacific. The former state is called La Niña and the latter El Niño. The La Niña state is preserved due to westward surface wind stress. The transition from the La Niña state to the El Niño state corresponds to a rapid change in sea surface temperatures of the eastern equatorial Pacific (Fig 1.5). Although this ENSO mechanism is not yet fully understood, it is widely accepted that during ENSO the evolution of anomalous condition results from a positive feedback between the tropical ocean and the tropical atmosphere. Important seems to be the adjustment of the equatorial ocean to changing winds. This adjustment is accomplished by certain types of waves, notably Rossby waves and Kelvin waves (see 2.5). These waves may play a key role in the ENSO phenomenon.

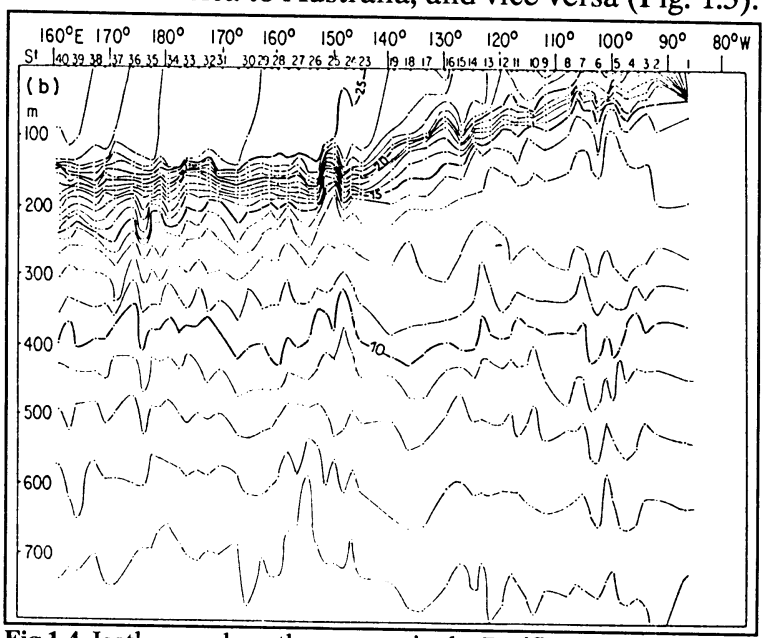

Fig.1.4. Isotherms along the equator in the Pacific Ocean (Lemason et Piton, 1968).

When the El Niño event is very strong it can cause great damage. In 1983 when the warm El Niño phase attained an exceptionally large amplitude, this caused devastating droughts over the western tropical Pacific, torrential floods over the eastern tropical

Pacific and damaging weather patterns over various parts of the world (Philander, 1991). The Southern Oscillation has its largest signature over the tropical Pacific and Indian Oceans, but it affects oceanic and atmospheric conditions globally. Observational studies have shown that a tight link between the Asian/Australian monsoon and the atmosphere/ocean system of the tropical Pacific exists. The interannual variability of Asian summer monsoon also has proved to be strongly influenced by the winter and spring snow cover over the Eurasian continent. So theoretical and observational evidence suggests that the coupled ocean/atmosphere system in the tropical Pacific combined with the Asian monsoon system is one of the major climate systems on the earth (Yasunari, 1991). From an oceanographic point of view El Niño is caused by changes in the surface winds over the tropical Pacific. So to explain El Niño it is necessary to explain how the ocean adjusts to the changes in the surface winds (Philander, 1990). The equatorial turbulent ocean boundary layer, which has its own specific properties, is a very important link in this process.

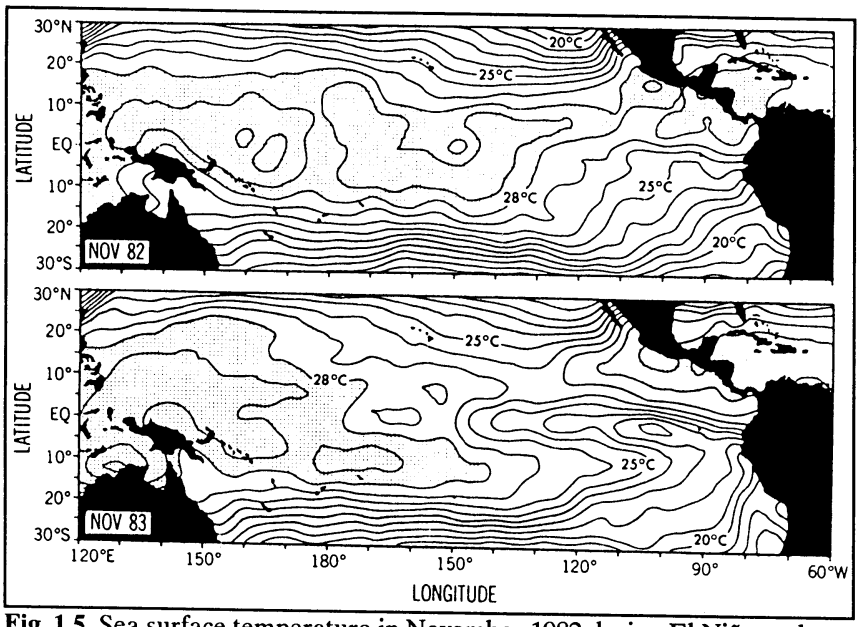

Fig. 1.5. Sea surface temperature in November 1982 during El Niño and one year later without an El Niño event (La Niña), (Philander, 1991).

1.3 Coupled Ocean Atmosphere models

Because of the possible devastating effects of an El Niño event it would be desirable to be capable to predict it. A great variety of approaches dealing with ENSO prediction already exists. They range from purely empirical schemes, using extratropical(!) atmospheric data as predictors, to coupled ocean-atmosphere models (COGM's). These COGM's, that try to be as complete as possible, have lots of difficulties. Many of them exhibit a slow drift from climatology, or a fast adjustment leading to a state with an overly weak or overly strong cold tongue (Neelin et al., 1991). By the "cold tongue" is meant the region of the eastern equatorial Pacific that has relatively cold surface temperatures (See Fig 1.5 for November 1983). These difficulties with CGCM's are not surprising because the models employ a great number of assumptions in parameterizing complex processes. Among processes poorly represented in the Ocean General Circulation Models (OGCM's) are nonlinearity of equatorial upwelling and surface

current/undercurrent dynamics (Neelin et al., 1991), which will be discussed in chapter 2 and chapter 7.

This study has the goal to obtain a deeper understanding of how the parameterization of vertical turbulence affects these equatorial dynamics (i.e. the surface current/undercurrent dynamics and the equatorial upwelling). Attention will be paid to the ocean part of the system only.

In chapter 2 some known and assumed physical processes influencing equatorial dynamics will be discussed; chapter 3 contains the theoretical fundaments on which this study was based; chapter 4 gives a description of the OGCM, with which the numerical experiments were conducted; in chapter 5 the mixing schemes are described; chapter 6 contains the results and in chapter 7 these results will be interpreted. Finally chapter 8 contains some concluding remarks.

2 Principal physical processes

In this chapter we will take a look at some physical processes and equatorial dynamics that influence the behaviour of the equatorial ocean boundary layer. This chapter is meant to give a first acquantance with some definitions, boundary values and equatorial phenomena that are or seem to be important for the description of the dynamics of the equatorial Pacific. Several topics treated here will return in chapter 6 and 7.

2.1 Turbulence

Turbulence is rotational flow, characterized by a great number of excited degrees of freedom. The vorticity of the flow is of great importance in turbulence mechanics. A compact definition for turbulence could be "chaotic vorticity" (Nieuwstadt, 1989). It gives rise to a cascade process, in which small vortices (eddies) are generated by larger ones. This cascade over the entire scale spectrum leads to the transfer of kinetic energy toward molecular scales.

The turbulence structure with the greatest dimensions is called the macrostructure. This macrostructure can be described with a lengthscale l and a velocity scale u for the largest eddies. These scales are directly linked up with the geometry of the flow (Tennekes and Lumley, 1972). In case of the upper ocean the lengthscale could for example be the depth of the turbulent layer, and the velocity scale could be the friction velocity u_*. These quantities will be discussed later. The main processes that introduce vorticity in the ocean are instability processes, which are caused by convection, shear in the mean flow and wavebreaking processes (see below). Figure 2.1 shows an example of such an instability process - the so-called Kelvin-Helmholtz instability. Instability processes similar to this one make the large scale eddies fall apart into smaller eddies. This cascade process continues until the micro scales are reached, at which the kinetic energy is converted into heat (molecular kinetic energy). Typical values for the length of this microscale are for the ocean and atmosphere of the order of a millimeter (Gill, 1982).

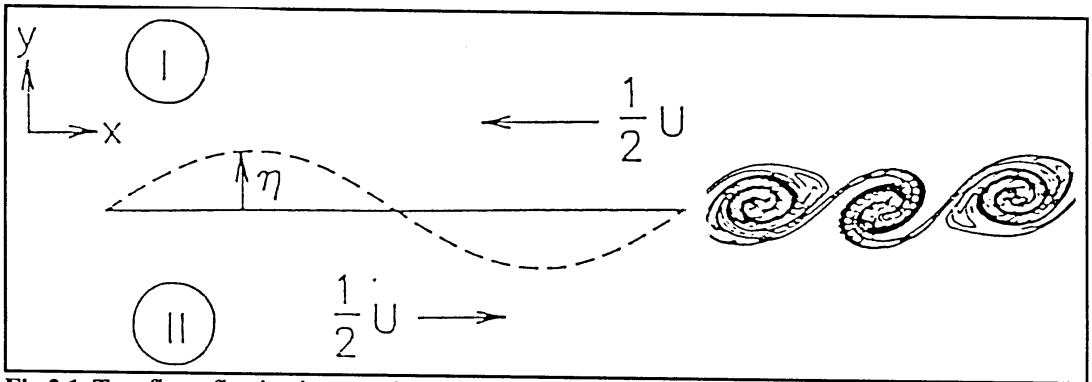

Fig.2.1. Two flows flowing in opposite direction give rise to a socalled Kelvin-Helmholtz instability (Nieuwstadt, 1991).

Convection

Convection is the (unstable) transport of a property by the transport of the matter which posseses that property. In the ocean the motions that give rise to convective processes are caused by an instable density stratification that results from cooling of the ocean surface or by salt accumulation in surface waters during periods of intensive evaporation. It is one of the most important and least understood mechanisms by which heat is transferred between the atmosphere and the ocean. Useful in discussing convection is the Brunt-Väisälä or buoyancy frequency, N, which is a measure for the density stratification and for seawater is specified by

$$N^2 = g\left(\frac{\alpha\partial\theta}{\partial z} - \frac{\beta\partial S}{\partial z}\right) \approx -g\rho_0^{-1}\frac{\partial\rho}{\partial z} = \frac{\partial b}{\partial z} \quad . \qquad (2.1)$$

Here g is the acceleration of gravity; Θ the potential temperature; $\alpha = -\partial(\ln\rho)/\partial\Theta$ the coefficient of thermal expansion and $\beta = \partial(\ln\rho)/\partial S$ the coefficient of haline contraction. ρ is the density and ρ_0 denotes a reference density. The buoyancy acceleration b is defined by

$$b = -g\frac{(\rho - \rho_0)}{\rho_0} \quad . \qquad (2.2)$$

The mechanisms that do effect the density stratification of the top layer of the ocean (i.e. the heat and fresh water fluxes) will be discussed in sections 2.2 and 2.3.

Wind stress and shear flow

Wind transfers momentum to the ocean. It is generally assumed that most of the atmospheric momentum flux is first absorbed by the surface wave field. It cannot be retained there, and it is quickly transported to the underlying ocean by wavebreaking processes (Müller and Garwood Jr., 1988). This momentum flux produces ocean currents, that generate shear flow instabilities. These instabilities will give rise to turbulence as described above. More about this momentum flux in section 2.4.

Entrainment

Entrainment is the generation of turbulence in a laminar flow by an adjacent turbulent flow. Eddies that are produced by convection and/or shear flow instabilities are sometimes powerful enough to penetrate the laminar flow of the ocean interior below the turbulent surface layer. Non-turbulent flow is captured by the turbulence and the turbulent domain will expand.

2.2 Heat fluxes

In this section the parameterizations of heat and fresh water fluxes at the ocean surface will be discussed. For a more thorough description see Gill (1982).

The heat balance of the ocean

Due to the solar radiation absorbed at the ocean surface the ocean heats up. In response to this warming, the ocean surface reaches such a temperature that the net losses of heat equal the gain from solar radiation. The total upward flux Q of heat from the ocean can be written as follows,

$$Q = Q_B + Q_E + Q_S - Q_I \qquad (2.3)$$

where Q_B is the net upward flux of long wave radiation; Q_E the upward latent heat flux, i.e. the heat loss due to evaporisation; Q_S is the upward sensible heat flux due to turbulent air motion and Q_I is the rate of absorption of solar radiation. These quantities will be described below.

Solar heating

Almost all the solar radiation received by the ocean is absorbed in its top 100m. The molecular absorption of radiation varies strongly with wavelength. The solar and atmospheric long wave radiation are absorbed in the top centimetre of the ocean, while the blue green sunlight can sometimes reach deeper than 100m. The vertical distribution of heating therefore not only depends on the clearness of the water - due mainly to the presence of plankton, tiny plants and animals - but also on the spectrum of the surface irradiance. The rate of solar heating decreases exponentially with depth. (Often it is assumed that all the incoming radiation is absorbed at the ocean surface.) The irradiance is dependent on the season, time of day, and properties of the overlying air like humidity and cloudiness. The rate Q_I of absorption of solar radiation is usually calculated as a product of (*i*) Q_{I0}, the net downward flux of solar radiation just above the surface in cloudless conditions. (this is usually 0.7 - 0.75 of the flux incident at the top of the atmosphere), (*ii*) $(1 - \alpha_s)$, where α_s is the surface albedo and (*iii*) a correction factor for cloud effect with n_c the fraction of the sky covered by cloud. An example of such a formula is

$$Q_I = Q_{I_0}(1 - \alpha_S)(1 - 0.7 n_c) \quad . \qquad (2.4)$$

Energy release to the atmosphere

There are three ways in which the ocean releases heat to the atmosphere: by thermal radiation, by evaporation (latent heat) and by turbulent transport (sensible heat).

Thermal radiation

The thermal radiation depends on the temperature of the surface skin of the ocean. It is unaffected by the properties of the overlying air. Often, however, it is convenient not to consider the rate of radiative cooling of the ocean, but its excess over the heating of the ocean by thermal radiation. This excess, known as the net long wave radiation at the sea surface, varies both with the ocean skin temperature and the atmospheric temperature.

Q_B is usually calculated as a product of (*i*) σT_s^4, which is the flux emitted by a black body of temperature T_s, $\sigma = 5.7 \times 10^{-8}$ $Wm^{-2}K^{-4}$ being the Boltzmann constant, (*ii*) a correction factor 0.985 for departure of the ocean surface from blackbody behaviour, (*iii*) a correction factor for back radiation by the atmosphere in the absence of clouds and (*iv*) a correction factor for the effect of clouds. An example of such a formula is

$$Q_B = 0.985\sigma T_s^4 (0.39 - 0.05 e_a^{1/2}) (1 - 0.6 n_c^2) \qquad (2.5)$$

where e_a is the vapor pressure of water at the standard height.

Latent heat

The latent heat flux depends on the saturated vapour pressure of the ocean (a function of temperature and salinity) and the surface humidity pressure in the mixed layer of the atmosphere.

Q_E can be written as L_vE, with E the evaporation rate and $L_v = 2.5 \times 10^6$ Jkg^{-1} the latent heat of vaporization of water. Q_E is usually calculated from a bulk-type formula similar to

$$E/\rho_a = c_E u (q_s - q_a) \qquad (2.6)$$

with ρ_a the density of the air, u the wind speed, q_a the specific humidity (mass of water vapor per unit mass of of air) at the standard level, q_s the specific humidity at the sea surface and c_E a dimensionless coefficient.

Sensible heat

The sensible heat flux depends on the temperature difference between the two mixed layers, on the wind speed and on the spectrum of waves at the interface. Similar to the latent heat Q_S can be approximated as

$$Q_S/\rho_a c_p = c_H u (T_s - T_a) \qquad (2.7)$$

with $\rho_a c_p$ the heat capacity of air per unit of volume, c_H a dimensionless coefficient, T_s the sea temperature and T_a the air temperature.

2.3 The buoyancy flux

Vertical instability is mostly enhanced by density contrasts. In the ocean these density contrasts are due to both temperature and salinity differences. These are created by the fluxes of heat and fresh water at the ocean surface whose combined effect on the buoyancy is called the buoyancy flux B (the buoyancy is the quantity for the weight per unit of volume, $-g\rho$), which is given by

$$B = c_w^{-1} g\alpha Q + g\beta (E - P) S \qquad (2.8)$$

where Q is the net upward heat flux, E the evaporation rate, P the precipitation rate, c_w the specific heat of water, S the surface salinity, α the thermal expansion coefficient of seawater at the surface, and β the corresponding coefficient for salinity, as described in section 2.1. An alternative expression may be obtained by using (2.3), which gives

$$B = c_w^{-1} g\alpha (Q_B + Q_S - Q_I) - g\beta SP + g(c_w^{-1} \alpha L_v + \beta S) E \quad . \qquad (2.9)$$

This expression shows that evaporation decreases the buoyancy in two ways, that is by cooling and by increasing salinity at the ocean surface.

2.4 The momentum flux

The flux of momentum from the atmosphere to the ocean mostly is absorbed by the surface gravity waves, causing instability and breaking of the waves. Its evaluation stricktly requires a specification of the full wave spectrum but often this is simplified. Usually the normal component of the momentum flux tensor (wind stress τ) is parameterized with the bulk aerodynamic formula

$$\tau = C_d \rho |U_{10}| U_{10} \qquad (2.10)$$

with U_{10} the wind at a standard height of 10m derived from ship observations and the drag coefficient C_d determined empirically.

Ekman transport

The upper layer motion of the ocean resulting from a steady momentum flux is not in the direction of the wind but at a substantial angle to it (to the right in the northern hemisphere, to the left in the southern). Ekman (1905) showed that this behaviour resulted from the Coriolis force. When the wind blows over the surface, it causes a frictional stress in the direction of the wind. Immediately the Coriolis force acts at right angles to the direction of motion, tending to cause the flow to be redirected to the right (in the northern hemisphere) or to the left (in the southern hemisphere) of the wind direction. At the same time, as the surface parcel commences to move, a retarding friction stress develops between it and the next layer below. This retarding force on the bottom of the the parcel is opposite to that of the water motion. In the simple application of the theory a steady state develops in which the surface water velocity is at 45° to the right (left) of the wind direction. A similar argument can be applied to succesive layers beneath the surface layers and each of these will move at a slower speed and in a direction further to the right of the top layer water motion, this velocity structure is called the Ekman spiral (Fig. 2.2).

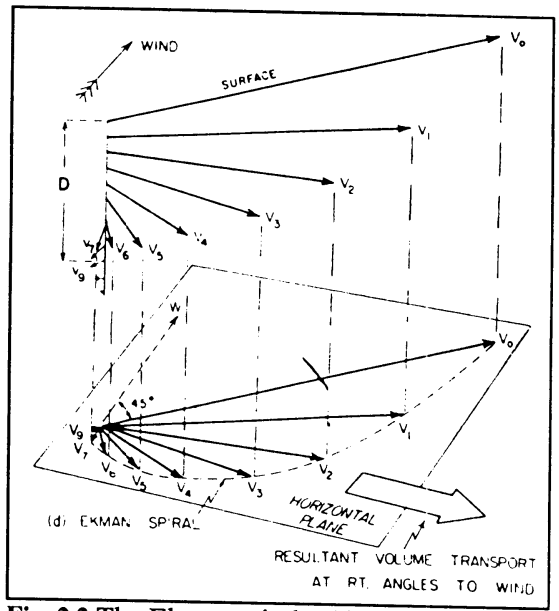

Fig. 2.2 The Ekman spiral, whith D the depth of the Ekman layer (Pickard and Emery, 1990).

It can be shown that the resultant volume transport in the Ekman layer is at right angles to the wind direction. This is called the Ekman transport (Fig. 2.3).

2.5 Equatorial dynamics

Equatorial dynamics are quite different from the non-equatorial. This is not only because the lateral component of the Coriolis force disappears at the equator, but also because the fact that its variation with latitude has a maximum there.

This causes phenomena like the equatorial undercurrent, the intertropical convergence zone (ITCZ), equatorial upwelling, equatorial trapping and a variety of equatorial waves. These will be explained below.

Tropical air circulation

A simple presentation of the tropical air motions is the following: at the equator hot air rises and moves north or southward losing much of its energy by radiation; it descends at the tropics and returns back to the equator along the surface. This meridional circulation cell is called the Hadley cell. The region with rising air is, because of the convergent air motion near the surface, called the intertropical convergence zone (ITCZ). It appears that the only way in which heat can effectively been brought from the surface to the upper troposphere in the ITCZ is through pseudo-adiabatic ascent in the

cores of large cumulonimbus clouds (Holton, 1979). This view of the ITCZ as a narrow band of vigorous cumulus convection has been confirmed by observations. On satellite pictures the narrow regions of convergence can be seen as lines of clouds near the equator. They tend to be found at the latitude at which the sea-surface temperature is maximal and to migrate seasonally with this maximum.

In the equatorial Pacific besides this meridional Hadley circulation another circulation exists: above the warm water of the western Pacific moisture laden air rises and above the relatively cold eastern Pacific dry air descends. The trade winds at the surface link these two regions. This zonal cell is called the Walker Circulation. The Walker Circulation is weak in March and April when sea level pressure gradients tend to be small over the equatorial Pacific.

The Southern Oscillation is a perturbation to these two connected thermal circulations (Hadley and Walker circulation) and is associated with fluctuations in the intensity, and the positions of rising moist air, i.e. the positions and intensity of low pressure areas. So the tropical circulation is by no means constant and is subject to pronounced changes at many time scales.

The Pacific equatorial current system

The trade winds are the most important driving force behind the equatorial ocean currents systems. They give rise to an off-equatorial Ekman transport. At the equator, where there is no Coriolis force, the water is allowed to flow downwind.

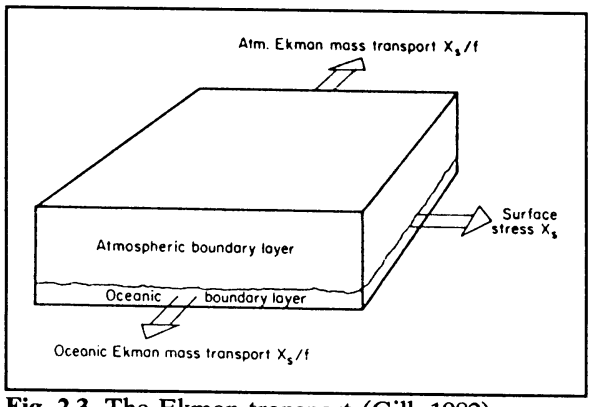

Fig. 2.3. The Ekman transport (Gill, 1982).

Here we will pay attention in particular to the Pacific equatorial current system. This system is recognized to include at least four major currents, three of which extend to the surface and one of which is below the surface (Fig. 1.4). The three upper-layer currents are the westward-flowing North Equatorial Current (between 20° N to 8° N), the westward South Equatorial Current (from 3° N to 10° S) and the narrower North Equatorial Countercurrent flowing to the east, between them. The surface current system is driven by the trade winds and is asymetrical about the equator because the trade wind system is asymetrical (Pickard and Emery, 1990). The current below the surface is found right at the equator and is called the equatorial undercurrent (EUC), (see below).

The equatorial undercurrent

The equatorial undercurrent is a major feature of the equatorial ocean circulation, in particular in the Pacific and the Atlantic ocean. It is a strong narrow eastward current found in the regions of strong density gradients below the mixed layer. It has its core close to the equator (within a degree). Its vertical thickness is around 100 m and its half width is a degree of latitude. The maximum current is typically 1 ms^{-1}. The undercurrent is induced by a pressure gradient along the equator which is balanced by the easterly

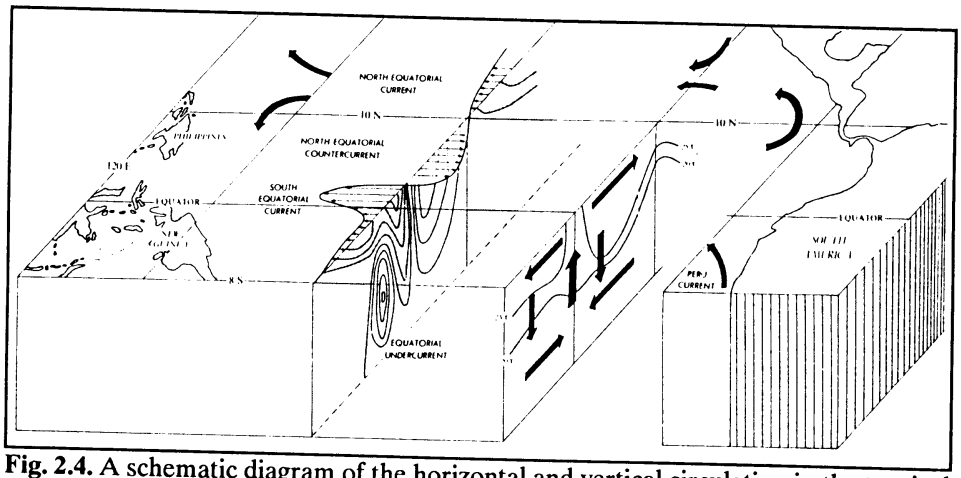

Fig. 2.4. A schematic diagram of the horizontal and vertical circulation in the tropical Pacific Ocean (Philander, 1990).

windstress. Because of the stratification this gradient only exists in the the upper layers. Away from the equator, such a gradient would cause a geostrophic flow towards the equator. At the equator the lateral component of the Coriolis force disappears and the current is allowed to flow directly down the pressure gradient.

North and south of about 1.5° latitude the Coriolis force, associated with this eastward flow, can balance the eastward pressure gradient. It is only very near to the equator that that the Coriolis effect is so weak that the Undercurrent is possible. Although the lateral component of the Coriolis force vanishes at the equator its variation with latitude has a maximum there, which tends to stabilize the current (Philander, 1990).

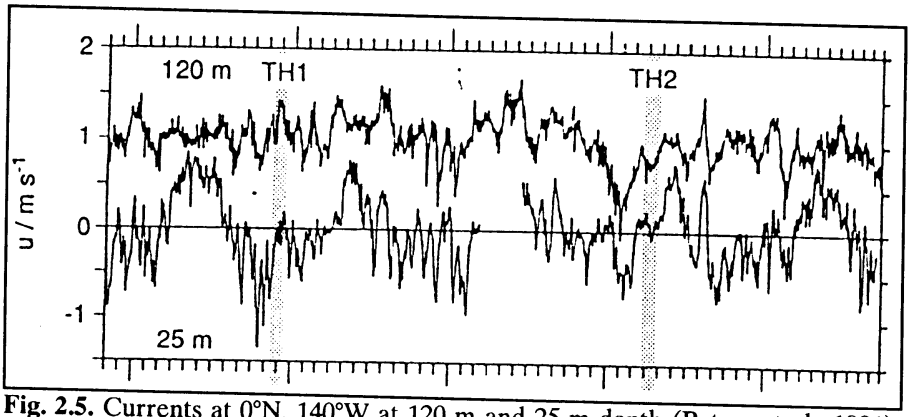

Fig. 2.5. Currents at 0°N, 140°W at 120 m and 25 m depth (Peters et al., 1991).

Equatorial upwelling

As one goes away from the equator, Coriolis effects become important. In the surface layer with a west-ward directed wind, the Ekman transport will be away from the equator on both north and south sides. Below the surface layer there has to be convergence (flow towards the equator) to balance the surface divergence. Due to the divergence at the surface there is an upward water motion right at the equator. This is called equatorial upwelling.

Equatorial waves

A very important property of the equatorial zone is that it is able to "trap" certain types of waves like Rossby waves, which are due to the earth's rotation, and Kelvin waves. Rossby and Kelvin waves are internal waves, i.e. they run on stratification differences in the subsurface ocean. They have wavelength's of several thousands of kilometres and a speed that depends on the vertical density stratification of the water, and in case of the Rossby waves the distance from the equator. The fast Kelvin waves can cross the Pacific basin in about two months. The three to five year time scale of ENSO could involve these wave processes. Theories involved with these waves are based on the idea of Rossby waves that are reflected at the western boundary (Australia/Indonesia) as equatorial Kelvin waves. For a more thorough description of these waves see Gill (1982) or Philander (1990).

Equatorial turbulence

Because of the existence of the equatorial undercurrent, the equatorial turbulent boundary layer is different from its off-equatorial counterpart. At the equator a turbulent layer overlies a turbulent pycnocline (i.e. the sharp gradient in density between the surface layer and the ocean interior). The pycnocline in the off-equatorial regions is typically almost laminar (Peters, 1990). So at the equator, beneath an almost homogeneous turbulent surface layer (mixed layer), a layer with stratified turbulence exists. Due to the breaking of internal waves, this layer often loses its continuous character and the turbulence becomes patchy. This is anologous to the vertical diffusion in the stable atmosphere (Pleune, 1990).

3 Theory

In this section the basic equations that govern the changes in the ocean (and the atmosphere) are summarized. Some turbulence- and ocean mixed layer theory is treated. For a fast reading of this report this chapter may be skipped. From now on the Einstein summation notation is employed (see also Stull, 1988).

3.1 The governing equations

For a derivation of the following equations see Gill (1982) or Batchelor (1967).

The mass conservation equation

$$\frac{D\rho}{Dt} + \rho\frac{\partial u_i}{\partial x_i} = 0 \quad . \tag{3.1}$$

In this equation $u_i(x_j,t)$ represents the velocity field in a righthanded Cartesian frame (x_1,x_2,x_3), and ρ is the density. Where $D/Dt = \partial/\partial t + u_j(\partial/\partial x_j)$; the so-called material derivative. The equation describes the conservation of mass. If we consider the fluid to be incompressible we get

$$\frac{\partial u_i}{\partial x_i} = 0 \quad , \tag{3.2}$$

which is the continuity equation.

The momentum equation

The equation of motion for a fluid is the Navier Stokes equation, usually shortened to

$$\rho\frac{Du_i}{Dt} = \rho f_i - \frac{\partial p}{\partial x_i} + \mu\frac{\partial^2 u_i}{\partial x_j{}^2} \quad , \tag{3.3}$$

where f_i is the external force, p the pressure, μ the dynamic viscosity. In a rotating frame under influence of gravity, the equation yields,

$$\frac{Du_i}{Dt} + 2\epsilon_{ijk}\Omega_j u_k = g_i - \frac{1}{\rho}\frac{\partial p}{\partial x_i} + \nu\frac{\partial^2 u_i}{\partial x_j{}^2} \quad , \tag{3.4}$$

with $g_i = (0,0,-g)$, the gravity acceleration, Ω_i the angular velocity of the rotation and with $\nu = \mu/\rho$ the kinematic viscosity.

The heat equation

The heat equation is given by

$$\rho c_p \frac{DT}{Dt} - \alpha \frac{Dp}{Dt} = \frac{\partial}{\partial x_j}\left(k \frac{\partial T}{\partial x_j} - R_i\right) + Q_{ih} \quad . \tag{3.5}$$

In this equation T is the temperature, c_p the heat capacity of seawater, $\alpha = (1/\rho)\,\partial\rho/\partial T$ the thermal expansion coefficient, k the thermal conductivity, R_i the radiative flux density of energy and Q_{ih} gives the rate of (internal) heating per unit of volume due to latent heat release, chemical reaction or viscous dissipation.

The concentration equation for salt

$$\frac{DS}{Dt} = \frac{\partial}{\partial x_j}\left(\kappa_S \frac{\partial S}{\partial x_j}\right) \quad . \tag{3.6}$$

This equation describes the molecular salt diffusion. S is the salinity and κ_S is the diffusivity coefficient for salt.

The equation of state

The density of seawater should be a function of the pressure, temperature and the salinity.

$$\rho = \rho(p, S, T) \quad . \tag{3.7}$$

When we consider the fluid to be incompressible, the density is only a function of temperature and salinity. For example, in the OGCM used in this study the equation of state has the following form

$$\rho = \rho_0 + A(T - T^*)^2 + BS \quad , \tag{3.8}$$

with ρ_0 = 1001.32630 kg/m3, A = -0.00471 kg/m^{3}K^2, B = 0.77390 kg/m^3 per promille and T^* = -7.73508° C (Allaart, Kattenberg 1990).

3.2 The Boussinesq approximation

For simplicity the so-called Boussinesq approximation is applied, which defines a reference state with pressure p_0 and density ρ_0. The reference state has to satisfy the equations of motion of a fluid at rest. The actual state is now conceived as a departure from this reference state with pressure $p_0 + p$ and density $\rho_0 + \rho$. With the hydrostatic equation for a fluid at rest $\partial p_0/\partial x_3 = -g\rho_0$, substitution in (3.4) gives

$$\frac{Du_i}{Dt} + 2\epsilon_{ijk}\Omega_j u_k = \frac{\rho}{\rho_0} g_i - \frac{1}{\rho_0}\frac{\partial p}{\partial x_j} + \nu\frac{\partial^2 u_i}{\partial x_j^2} \quad , \qquad (3.9)$$

This approximation treats the density as a constant, except when it appears in the buoyancy force term.

The heat equation (3.5) , when we ignore internal heat changes, and when we ignore the second left hand term, yields

$$\frac{DT}{Dt} = \frac{\partial}{\partial x_j}\left(\kappa_T \frac{\partial T}{\partial x_j}\right) \quad , \qquad (3.10)$$

with $\kappa_T = k/\rho c_p$ the thermal diffusivity coefficient. Together with the continuity equation (3.2) and the diffusion equation for salt (3.6) we have now the Boussinesq equations for seawater. With the linearized equation of state (3.11) these equations form the basis for the description of ocean dynamics. This linearization is written as follows

$$\frac{\rho - \rho_0}{\rho_0} = -\alpha(T - T_0) + \beta(S - S_0) \quad . \qquad (3.11)$$

Here α and β are the coefficients that decribe the logarithmic expansion of ρ as functions of T and S, as in section 2.1.

3.3 Reynolds decomposition

In order to consider turbulent processes we will employ the Reynolds decomposition, that is we split up an instantaneous variable into a mean and a fluctuating part. For example

consider the instanteneous velocity component u_i

$$u_i = \overline{u}_i + u_i' \quad , \tag{3.12}$$

where the overbar indicates the ensemble mean of a realisation, and the prime the fluctuation. If we apply the same procedure to the density ρ and the pressure p, and use equation (3.4) we get

$$\begin{aligned} &\frac{\partial \overline{u}_i}{\partial t} + \frac{\partial \overline{u}_i \overline{u}_j}{\partial x_j} + 2\epsilon_{ijk}\Omega_j \overline{u}_k = \\ &\frac{\overline{\rho}}{\rho_0} g_i - \frac{1}{\rho_0}\frac{\partial \overline{p}}{\partial x_j} + \nu \frac{\partial^2 \overline{u}_i}{\partial x_j^2} - \frac{\partial}{\partial x_j}\overline{u_i' u_j'} \quad , \end{aligned} \tag{3.13}$$

for the mean part of u_i, and for the fluctuating part

$$\begin{aligned} &\frac{\partial u_i'}{\partial t} + \overline{u}_j \frac{\partial u_i'}{\partial x_j} + u_j' \frac{\partial \overline{u}_i}{\partial x_j} + u_j' \frac{\partial u_j'}{\partial x_j} + 2\epsilon_{ijk}\Omega_j u_k' \\ &- \frac{\partial}{\partial x_j}\overline{u_i' u_j'} - \frac{\rho'}{\rho_0} g_i - \frac{1}{\rho_0}\frac{\partial p'}{\partial x_i} + \nu \frac{\partial^2 u_i'}{\partial x_j^2} \quad . \end{aligned} \tag{3.14}$$

Equivalently, when applying Reynolds decomposition to (3.10), considering κ_T to be homogeneous, we find the set of equations

$$\frac{\partial \overline{T}}{\partial t} + \overline{u}_j \frac{\partial \overline{T}}{\partial x_j} = \kappa_T \frac{\partial^2 \overline{T}}{\partial x_j^2} - \frac{\partial}{\partial x_j}\overline{u_j' T'} \tag{3.15}$$

$$\frac{\partial T'}{\partial t} + \overline{u}_j \frac{\partial T'}{\partial x_j} + u_j' \frac{\partial \overline{T}}{\partial x_j} + u_j' \frac{\partial T'}{\partial x_j} - \frac{\partial}{\partial x_j}\overline{u_j' T'} = \kappa_T \frac{\partial^2 T'}{\partial x_j^2} \tag{3.16}$$

For the salinity everything is exactly the same as for temperature with T in (3.15) and (3.16) replaced by S. If we now compare the equations (3.13) and (3.15) with the original equations (3.9) and (3.10) we see that there are two new terms involved in these equations: $\langle u_i' u_j' \rangle$ and $\langle u_i' T' \rangle$, with the brackets, like an overbar, indicating the mean. These are called Reynolds terms and can be interpreted respectively as a flux of momentum and a flux of temperature (salinity). Due to these new unknowns in the equations for $\langle u_i \rangle$ and $\langle T \rangle$ the number of unknowns becomes greater than the

number of equations. We need an extra relation to overcome this problem. This is called the closure problem.

3.4 K-theory

One method to overcome this closure problem is by applying K-theory. The turbulent fluxes $<u_i'u_j'>$, $<u_i'T'>$ and $<u_i'S'>$ are considered to be proportional to the local gradients of respectively momentum, heat and salinity.

$$-\overline{u_i'u_j'} = K_m \frac{\partial \overline{u}_i}{\partial x_j} \quad ; \tag{3.17}$$

$$-\overline{u_j'T'} = K_T \frac{\partial \overline{T}}{\partial x_j} \quad ; \tag{3.18}$$

$$-\overline{u_i'S'} = K_S \frac{\partial \overline{S}}{\partial x_j} \quad . \tag{3.19}$$

K_m is here is the socalled eddy viscosity and K_T and K_S are the eddy diffusivities for heat and salinity.

3.5 The turbulence kinetic energy equation

The turbulence kinetic energy is defined as $e = 1/2 < u_i'^2 >$. An expression for this turbulence kinetic energy can be obtained by multiplying equation (3.14) by u_i' and average. The resulting expression is

$$\frac{De}{Dt} = -\overline{u_i'u_j'} \frac{\partial \overline{u}_i}{\partial x_j} + \frac{\overline{u_i'\rho'}}{\rho_0} g_i + \frac{\partial}{\partial x_j} \left(-\overline{u_j'e'} - \frac{1}{\rho_0} \overline{p'u_j'} + \nu \frac{\partial e}{\partial x_j} \right) - \epsilon \tag{3.20}$$

the so called turbulence kinetic energy equation where

$$\epsilon = \nu \overline{\left(\frac{\partial u_i'}{\partial x_j} \right)^2} \quad . \tag{3.21}$$

In this equation e' = 1/2 $u_i'^2$. The term at the left hand side represents the change of turbulence kinetic energy per unity of mass at a point that moves with the mean flow. The term that takes account of the Coriolis effect disappears because of the summation over the three directions. It doesn't disappear when you look in one particular direction (see also chapter 5).

The first term at the right hand side of (3.20) expresses the energy that the mean flow provides to the turbulence by means of instability processes (see 2.1). If we consider the assumption (3.17) to be correct, it follows that for the first term we can write

$$-\overline{u_i' u_j'} \frac{\partial \overline{u}_i}{\partial x_j} - K_m \left(\frac{\partial \overline{u}_i}{\partial x_j} \right)^2 \geq 0 \quad , \qquad (3.22)$$

i.e. following the first order closure hypothesis, instability processes in the flow will always provide energy to the turbulence and will never extract energy from it.

The second term at the right hand side of (3.20) represents the influence of density effects on a turbulent flow. If this term is positive it causes an increase in turbulence kinetic energy, i.e. the buoyant acceleration supports the turbulent kinetic energy. If the term is negative, turbulence kinetic energy will be destroyed.

The third term at the right hand side of (3.20), the divergence term, represents the redistribution of turbulence kinetic energy within a volume V without a net increase or decrease of this energy. For this reason it is often called the transport term. It consists of three parts of which the first represents the transport by velocity fluctuations; the second the transport by pressure fluctuations and the third the transport by viscosity. For large Reynolds numbers, the viscosity part can be neglected.

The last term in (3.20) is always negative. It destroys the turbulence kinetic energy and is therefore called the dissipation. It represents the conversion of turbulence kinetic energy into heat by molecular viscosity. Because the gradients of u_i' are great at small scales and are small at large scales, it follows that this term is only active at the small scales.

So turbulence is produced at large scales and is destroyed at the small scales. The energy is transported from the large scale to the small scale by so called cascade processes. Due to instability processes large eddies fall apart in smaller eddies until these eddies reach the small scale (see 2.1). At this microscale, turbulence kinetic energy is converted into heat by molecular viscosity.

3.6 The Richardson number

Now let's go back to equation (3.20). When we simplify this equation by ignoring the transport term and considering horizontal homogeneity we can write

$$\frac{De}{Dt} = -\overline{u_i' u_3'} \frac{\partial \bar{u}_i}{\partial x_3} (1 - Ri_f) - \epsilon \quad , \tag{3.23}$$

with

$$Ri_f = \frac{\frac{\overline{u_3' \rho'}}{\rho_0} g}{\overline{u_i' u_3'} \frac{\partial \bar{u}_i}{\partial x_3}} \quad , \tag{3.24}$$

the Richardson flux number. When $Ri_f < 0$ we call the flow instable or convective, when $Ri_f > 0$ we call the flow stable. From (3.23) it follows that turbulence may die out ($De/Dt < 0$) when $Ri_f > 1$. Measurements however indicate that the turbulence already dies out for $Ri_f > 0.25$. It is however clear that the Richardson flux number is a measure for (shear)flow stability, (see also chapter 5).

3.7 The Niiler and Kraus description of ocean turbulence

If we assume lateral homogeneity for the ocean (3.20) reduces to

$$\frac{\partial e}{\partial t} = -\overline{u_\alpha' u_3'}\frac{\partial \overline{u}_\alpha}{\partial u_3} + \overline{u_3' b'} + \frac{\partial}{\partial x_3}\left(-\overline{u_3' e'} + \frac{1}{\rho_0}\overline{p' u_3'}\right) - \epsilon \quad . \quad (3.25)$$

With α equal to 1 or 2. With use of Reynolds decomposition as described before and with the assumptions that Q_{ih} and α are neglegible and that molecular effects can be ignored (Re >> 1), the heat equation reduces to

$$\frac{\partial \overline{T}}{\partial t} + \frac{\partial}{\partial x_3}\overline{u_3' T'} = -\frac{1}{\rho c_p}\frac{\partial Q_I}{\partial x_3} \quad (3.26)$$

The corresponding equation for salinity is

$$\frac{\partial \overline{S}}{\partial t} + \frac{\partial}{\partial x_3}\overline{u_3' S'} = 0 \quad . \quad (3.27)$$

With these latter two equations we can derive a conservation equation for the buoyancy

$$\frac{\partial \overline{b}}{\partial t} + \frac{\partial}{\partial x_3}\overline{u_3' b'} = -\frac{g\alpha}{\rho c}\frac{\partial Q_I}{\partial x_3} \quad . \quad (3.28)$$

To solve this set of equations (3.25 - 3.28) one has to find explicit expressions for the fluxes. In the following section the assumptions made by Niiler and Kraus (1977) will be discussed.

Assumptions

The main assumption is that, with respect to temperature, salinity and velocity, there exists a vertical uniform turbulent layer of depth h that is on top of the nonturbulent interior of the ocean. This allows us to integrate (3.25), (3.26), (3.27) and (3.28) from x_3=-h to the surface at x_3=0. The assumption of vertical uniformity permits representation of the bulk horizontal velocity, temperature and salinity of the layer as a function of exchanges with the air above and with the interior below. The system however is still not closed, because the time-dependent h has been introduced as a new

variable. In the absence of a mean vertical velocity the deepening of this mixed layer must be equal to the rate u_{3e} at which water is entrained from the interior below (see 2.1). Entrainment is associated with layer deepening. When the mixed layer becomes shallower, the entrainment must cease.

$$\begin{aligned} u_{3e} &\equiv \frac{dh}{dt} \qquad \text{for } dh/dt > 0 \ . \\ u_{3e} &\equiv 0 \qquad \text{for } dh/dt \leq 0 \ . \end{aligned} \tag{3.29}$$

To evaluate the integrals of (3.25 - 3.28) over the mixed layer we need to know the flux boundary conditions at the surface ($x_3=0$) and at the bottom interface ($x_3=-h$).

Flux boundary conditions at the sea surface

When we now go back to equation (2.9) we can write for the the second term at the right hand side, the turbulent buoyancy flux

$$\frac{\overline{u_i'\rho'}}{\rho_0} g \,]_{x_3=0} \equiv B_0 - \frac{B}{\rho_0} \ , \tag{3.30}$$

or, when we introduce the buoyancy acceleration as described in section 2.1, it yields

$$\overline{u_3'b'} \,]_{x_3=0} \equiv B_0 \ . \tag{3.31}$$

The momentum flux

Conform equation (2.10) we can write for the turbulent flux of momentum

$$\overline{u_\alpha' u_3'} \,]_{x_3=0} - \frac{\tau_\alpha}{\rho_0} \ , \tag{3.32}$$

with $\tau = \rho_0 u_*^2$. We also need an expression for the term in brackets in equation (3.25), the transport term: the flux of turbulence kinetic energy from the atmosphere to the ocean by pressure and velocity fluctuations. Near the sea surface this flux should be equal to the rate of working by the wind. This means that it has to be equal to the stress multiplied by a wind velocity. The problem is that we cannot measure this wind velocity without ambiguity at any particular height. We shall therefore describe the rate of

working as follows

$$(\overline{u_3'e'} + \rho_0^{-1}\overline{u_3'p'})\ ]_{z=0} = c_\mu u_*^3 \quad . \tag{3.33}$$

where c_μ is a matchable constant.

Flux boundary conditions at the bottom of the mixed layer

As already stated, it is assumed that at the bottom of the mixed layer there is no vertical advection. Moreover the effect of diffusion across the stable interface at the bottom of the mixed layer is neglected. So all mixing processes are associated with the entrainment of the lower fluid into the mixed layer. With these assumptions the boundary condition for the density flux assumes the form

$$\overline{u_i'\rho'} + u_{3e}\Delta\rho = 0 \quad , \tag{3.34}$$

or equivalently

$$\overline{u_3'b'}\ ]_{x_3=-h} + u_{3e}\Delta b = 0 \quad . \tag{3.35}$$

The symbols $\Delta\rho$ and Δb represent the assumed discontinuous changes of these quantities across the base of the mixed layer.

In the absence of entrainment the turbulent fluxes become zero at z = -h. This is when there is not enough turbulence kinetic energy available to overcome the stable stratification at the base of the layer and to produce any mixing with the lower water. One could say that in this case the mixed layer is assumed to be decoupled from the ocean interior.

The momentum flux boundary condition at the at the bottom of the mixed layer is not as simple. This is because internal waves can radiate momentum downwards through stable layers. This radiation stress is parameterized by Niiler and Kraus by the square of $<u_\alpha>$, multiplied by a generalized drag coefficient C (see also Gill (1982)), which should be a function of the particular density stratification in the fluid below the mixed layer. So the momentum flux boundary condition at the base of the mixed layer becomes

$$\overline{u_3'u_\alpha'}\ ]_{x_3=-h} + u_{3e}\bar{u}_\alpha = C\bar{u}_\alpha|\bar{u}_\alpha| \quad . \tag{3.36}$$

Finally, the boundary condition for the flux of mechanical energy can be established similarly in the form

$$(\overline{u_3'e'} + \frac{\overline{u_3'p'}}{\rho_0}) \quad]_{x_3=-h} + u_{3e}e = 0 \qquad (3.37)$$

The second term represents here the rate at which turbulence kinetic energy has to be supplied by the downward flux. This is to make the entrained water as agitated as the turbulent mixed layer water.

The integral relations

When we integrate equation (3.28) from a depth z to the surface, and again from a depth -h to the surface we can eliminate the time derivative db_0 / dt. After rearrangement one gets

$$\overline{u_3'b'} = B_0 + \frac{x_3}{h}(B_0 + u_{3e}\Delta b + \frac{g\alpha}{\rho c}Q_{I_0}) + \frac{g\alpha}{\rho c}Q_{I_0}(1 - e^{\gamma x_3}) \quad . \qquad (3.38)$$

where in order to deal with the effect of penetrating solar radiation we have set

$$Q_I = Q_{I_0}\exp(\gamma x_3) \qquad (3.39)$$

When we integrate (3.38) from the bottom of the layer $x_3 = -h$ to the surface $x_3 = 0$, we get

$$\int_{-h}^{0} \overline{u_3'b'}dx_3 = \frac{1}{2}hB_0 - \frac{1}{2}u_{3e}\Delta bh + \frac{g\alpha}{\rho c}Q_{I_0}(\frac{h}{2} - \frac{1}{\gamma}) \quad . \qquad (3.40)$$

This equation represents the rate of potential energy change associated with the lifting or lowering of the center of gravity of the water column. One can write

$$\Delta bh = c_I^2 \quad , \qquad (3.41)$$

with c_I the velocity of the long internal waves at the bottom interface (Gill, 1982). To find an explicit expression for the first right hand side term of equation (3.26), denoting the production of TKE by shear flow instabilities, is not very easy. The velocity gradient is obviously zero in the interior of the layer. To get round this difficulty Niiler and Kraus assumed a mixed layer as is represented schematically in figure 3.1. Now, using relation (3.37), we can write this integral as follows

$$\lim_{(h'-h)\to 0} \int_{-h'}^{-h} -\overline{u_3' u_\alpha'} \frac{\partial \bar{u}_\alpha}{\partial x_3} dx_3 \simeq \frac{1}{2} u_{3e} \bar{u}_\alpha^2 - \frac{1}{3} C \bar{u}_\alpha^3 \quad . \tag{3.42}$$

It is also likely that turbulence kinetic energy is produced by shear flow instabilities near the surface. The assumption is that the rate of generating of mean shearing motion near the surface will be equal to the rate of its destruction by mixing ($\sim u_*^3$). This makes it possible to consider the production term to be proportional to the rate of working by the wind. This effect can be accounted for by an adjustment of the proportionality factor c_μ in relation (3.34).

Using (3.41) and (3.42), we can now write the integral of equation (3.26) from $x_3 = -h$ to $x_3 = 0$ in the form

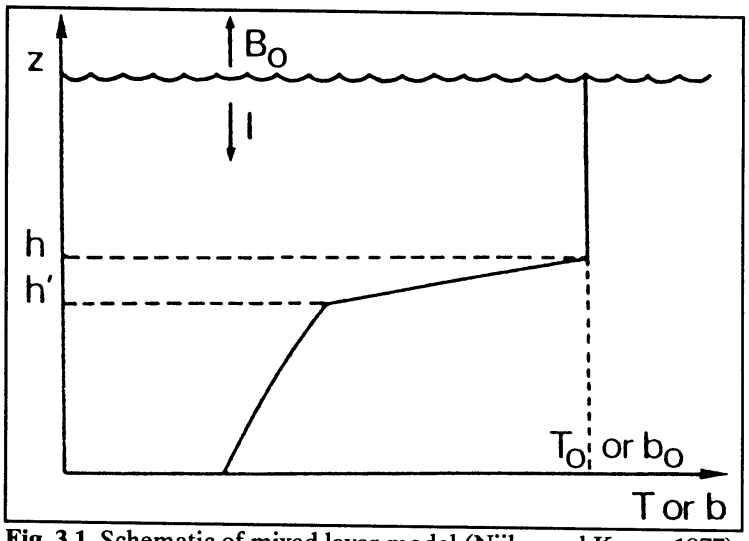

Fig. 3.1. Schematic of mixed layer model (Niiler and Kraus, 1977).

$$u_{3e}\left(e + \frac{1}{2} c_I^2 - \frac{1}{2} \bar{u}_\alpha^2\right) = c_\mu u_*^3 + \frac{1}{2} B_0 + \left(\frac{h}{2} - \frac{1}{\gamma}\right) \frac{g\alpha}{\rho c} Q_{I_0} - \frac{1}{3} C \bar{u}_\alpha^3 - \int_{-h}^{0} \epsilon \, dx_3 \quad . \tag{3.43}$$

Now we still have to find an expression for the dissipation term in (3.43). Niiler and Kraus assume this that the dissipation integral is composed of terms which are individually proportional to the active turbulence generating processes

$$\int_{-h}^{0} \epsilon \, dx_3 = (c_\mu - c_{\mu 1}) u_*^3 + (1 - c_\sigma) \frac{1}{2} u_{3e} \bar{u}_\alpha^2 + (1 - c_v) \frac{1}{2} h \frac{B_0 + |B_0|}{2} \quad , \tag{3.44}$$

with c_μ, c_σ and c_v proportionality factors. The last term in (3.44) should only differ from zero when turbulence is generated by surface cooling ($B_0 > 0$). Substitution of equation (3.44) into equation (3.43) yields

$$u_{3e}(e + \frac{1}{2}c_I^2 - \frac{1}{2}c_\sigma \bar{u}_\alpha^2) = c_{\mu 1}u_*^3 + \frac{h}{4}[(1+c_v)B_0 - (1-c_v)|B_0|] + (\frac{h}{2} - \frac{1}{\gamma})\frac{g\alpha}{\rho c_p}Q_{I_0} - \frac{1}{3}c\bar{u}_\alpha^3 \quad . \tag{3.45}$$

This expression is usually simplified by neglecting the first and the last term. Especially for the last term, which is related to the rate of working of the shear stress at the layer bottom, this may not be a good assumption (Niiler and Kraus, 1977). The equations becomes

$$u_{3e}(c_I^2 - c_\sigma \bar{u}_\alpha^2) = 2c_{\mu 1}u_*^2 + \frac{h}{2}[(1+ c_v)B_0 - (1-c_v)|B_0|] + (h - \frac{2}{\gamma})\frac{g\alpha}{\rho c_p} \quad . \tag{3.46}$$

The second right hand term is the same as hB_0 when $B_0 < 0$ and $c_v hB_0$ when $B_0 > 0$.

Special cases

We can say that when the mixed layer tends to become shallower $B_0 < 0$, implying $u_{3e}=0$. In this case one can find an expression for the mixed layer depth h. For $B_0 < 0$ we find

$$h = \frac{-2c_\mu u_*^3 + \frac{2}{\gamma}\frac{g\alpha}{\rho c}Q_{I_0}}{B_0 + \frac{g\alpha}{\rho c}Q_{I_0}} \quad . \tag{3.47}$$

If we also assume that $1/\gamma << 1$, i.e. the solar radiation is totally absorbed at the sea surface, we get for the mixed layer depth.

$$h = \frac{-2c_\mu u_*^3}{B_0 + \frac{g\alpha}{\rho c}Q_{I_0}} \quad , \tag{3.48}$$

For the case that $B_0 > 0$, as the layer deepens further, the contribution of the velocity shear decreases in inverse proportion to h^2. So this contribution tends to be small as h increase beyond a certain depth h_f. Omission of the velocity term at this stage changes equation (3.46) into

$$\frac{dh}{dt} = \frac{2c_\mu u_*^3}{h\Delta b} + \frac{c_v B_0}{\Delta b} \quad . \tag{3.49}$$

This was the equation used by Kraus and Turner (1967), which were pioneers in ocean turbulence modelling. See also Gaspar et al. (1988).

4 The tropical ocean model

The Ocean General Circulation Model (OGCM) used for this experiment was build by Marc Allaart. It is a primitive-equation, Cartesian-coordinate model with variable resolution. The model is described and documented by Allaart and Kattenberg (1990).

4.1 Description of the OGCM

The OGCM is a multilevel gridpoint model with a variable resolution:
i) zonally 2°
ii) meridionally from 0.5° near the equator to 2° at the north and south boundaries
iii) vertically: 13 layers from 20 m near the surface to 1000m at the bottom (4000 m)
The primitive equations with the usual assumptions for the hydrostatic and Boussinesq approximations (as described in chapter 3) are solved on an Arakawa-C grid (Fig. 4.1(a) and 4.1(b)) using second order finite difference techniques and are integrated foreward in time using a semi implicit time stepping algorithm. The time derivatives are changed into discrete timesteps of 7200 seconds (2 hours).

The region that the model covers is bounded by the longitudes 123° East and 80° West (with realistic landcontours), and by the latitudes ± 29° (Fig. 4.2). The "box" has a flat bottom at a depth of 4000 m. The boundaries and land contours are vertical walls. At these walls there is no flux of heat and salt and a "no-slip" condition for momentum.

IY/II						
4/7	$T_{1,4}$	$U_{1,4}$	$T_{2,4}$	$U_{2,4}$	$T_{3,4}$	$U_{3,4}$
3/6	$V_{1,3}$		$V_{2,3}$		$V_{3,3}$	
3/5	$T_{1,3}$	$U_{1,3}$	$T_{2,3}$	$U_{2,3}$	$T_{3,3}$	$U_{3,3}$
2/4	$V_{1,2}$		$V_{2,2}$		$V_{3,2}$	
2/3	$T_{1,2}$	$U_{1,2}$	$T_{2,2}$	$U_{2,2}$	$T_{3,2}$	$U_{3,2}$
1/2	$V_{1,1}$		$V_{2,1}$		$V_{3,1}$	
1/1	$T_{1,1}$	$U_{1,1}$	$T_{2,1}$	$U_{2,1}$	$T_{3,1}$	$U_{3,1}$
IX	1	1	2	2	3	3
II	1	2	3	4	5	6

4.1(a). Horizontal cross-section of the Arakawa-C grid, with U, T and V denoting sub-grids (Allaart and Kattenberg, 1990)

4.2 Forcing of the OGCM

The forcing of the OGCM was such that that the results are compatible with the TOGA-NEG (Tropical Ocean Global Atmosphere - Numerical Experimentation Group) ocean model intercomparison, i.e. the stress data are those of Hellerman and Rosenstein (1983) and thermal and salt forcings were taken from Oberhuber (1988), (see below). The project involves simulation of a seasonal cycle of the equatorial Pacific.

IZ/II					
3/6	V_3		V_3		V_3
3/5		Z_3		Z_3	
2/4	V_2		V_2		V_2
2/3		Z_2		Z_2	
1/2	V_1		V_1		V_1
1/1		Z_1		Z_1	
		⟶ x or y direction			

Fig. 4.1(b). Vertical cross-section of Arakawa-C grid (Allaart and Kattenberg, 1990).

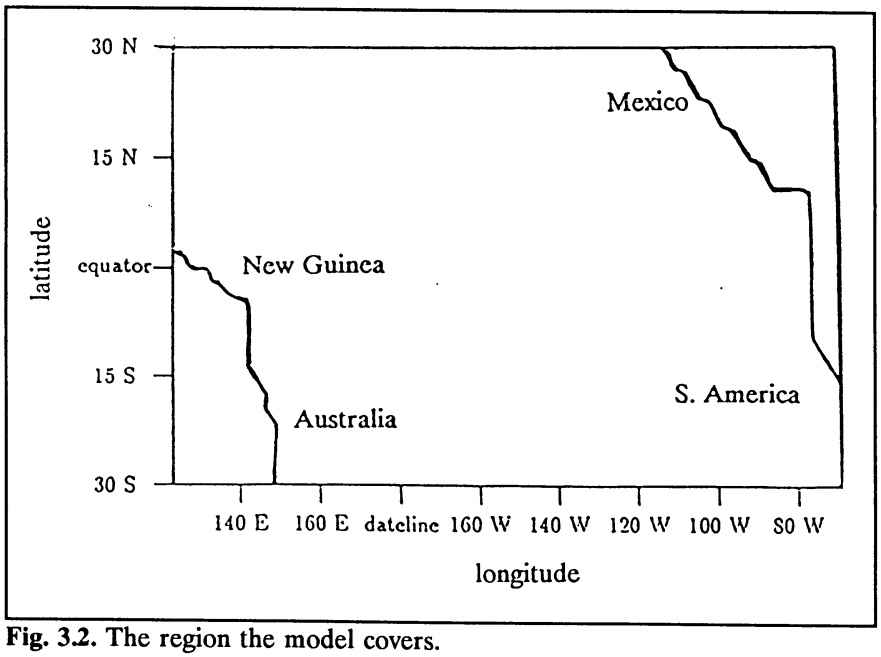

Fig. 3.2. The region the model covers.

Initialization and integration

The model was initialized with the climatological data (Levitus, 1982) for temperature and salinity and was spun up for five years. Data were gathered at the months 3, 6, 9, and 12 of the sixth year.

The bottom

At the bottom there is a stress layer. To avoid warming up of the lowest layer by diffusion and advection the bottom has a Newtonian forcing towards a temperature of 4°C. This mimicks the supply of cold water, from high-latitude deep water formation regions, that flows equatorward and wells up to form the (sub)tropical thermocline in the real ocean. The salinity has a Newtonian forcing towards Levitus data, (Levitus, 1982).

The surface

The model is forced with monthly mean data that are interpolated linearly at each timestep. The experimental setup is identical to the TOGA-NEG model intercomparison (see chapter 6). The model was forced with Hellerman windstress: monthly climatological values on a 2°x 2° grid but scaled by a factor 0.75, since experience using these fluxes suggest they may be to strong (WCRP, personal communication).

The surface heatflux is given by

$$Q = Q_{COADS} + \frac{dQ}{dT}\left(T_{model} - T_{COADS}\right) \quad , \qquad (4.1)$$

with Q_{COADS} the heat fluxes as provided by COADS, T_{COADS} the SST's as provided by COADS, T_{model} the surface temperature as computed by the OGCM and DQ/DT the atmosphere-ocean coupling coefficient as provided by COADS. COADS is the Comprehensive Ocean-Atmosphere Data Set (Oberhuber, 1988). The second right hand term of (4.1), a feedback term relaxing the model SST towards the mean COADS SST, from now on will be called the "heat flux error".

4.3 Subgrid-scale processes

There exists a wide spectrum of length (and time) scales in the ocean. They span from the subtropical gyres, with 10,000 km for the Kuroshio, down to eddy scales of about 100 km and of course to the scale of micro-turbulence (Oberhuber, 1992). Especially the subgrid-scale processes are mostly parameterized in an arbitrary way. It is a fundamental problem in ocean modelling (Bryan, 1991).

The large difference both in vertical and horizontal turbulence kinetic energy and in the model resolution requires a strongly anisotropic diffusivity tensor. We may split up the diffusivity terms that appear in equations (3.6), (3.9) and (3.10) in an horizontal and a vertical component. We can write for example equation (3.6) in the following form:

$$\frac{DS}{Dt} = d_H + \frac{\partial}{\partial z}\left(K\frac{\partial S}{\partial z}\right) \quad , \qquad (4.2)$$

with d_H the horizontal diffusion, which is mainly determined by the mesoscale eddy motions and is usually taken to be constant. Usually the horizontal diffusion is parameterized as follows

$$d_H = A_H \nabla_H^2 S \quad , \qquad (4.3)$$

where ∇_H is the divergence vector in the horizontal plane and A_H the horizontal diffusion coefficient (which usually is chosen to be (1-5) x 10^3 m^2s^{-1}, depending on numerical resolution). In this OGCM, with which the experiments described in this report were performed, the horizontal diffusion A_H = 5 x 10^3 m^2s^{-1}.

In high resolution models sometimes a biharmonic formulation is used, i.e. horizontal diffusion is written as

$$d_H = B_H \nabla_H^4 S \quad , \qquad (4.4)$$

This parameterization is more scale selective than (4.3), its physical basis is, however, weak. The parameterization for K (Eq. 4.2) is discussed in the next chapter.

5 Mixing formulations

This chapter contains a description of the vertical (one dimensional) mixing schemes that were tested in the OGCM for this study. Two main approaches to surface mixing are differential models and integral models.

5.1 Differential mixing models

In differential models the local exchange due to turbulent diffusion between two adjacent layers is parameterized. In this study K-theory (see section 3.4) is applied.

5.1.1 Richardson number dependent parameterizations

One possible parameterization of vertical eddy diffusivity and eddy viscosity is to make use of the Richardson number, which is a measure for vertical stability in a stratified flow (see section 3.6). Starting-point is the assumption that the eddy diffusivity and eddy viscosity are functions of the Richardson number.

$$\begin{aligned} K_m &= f(Ri) \\ K_{S,T} &= g(Ri) \end{aligned} \qquad (5.1)$$

The reasons for parameterizing turbulence in the form K(Ri) for regions with strong mean shear are merely pragmatic. The linear velocity profile that is observed in the equatorial regions, for example, is easily obtained using a Richardson number dependent mixing scheme. Also these schemes are appealing because of their simplicity and because of the ease with which they can be implemented in numerical models. The Richardson number dependent mixing schemes often are based on empirical relations.

Pacanowski and Philander

The most often used Ri-number dependent parameterization of eddy-viscosity/diffusivity is that developed by Pacanowski and Philander (1981). Following empirical studies they propose the following parameterization:

$$\begin{aligned} K_m &= \frac{\nu_0}{(1 + \alpha Ri)^n} + \nu_b \\ K_{S,T} &= \frac{K_m}{(1 + \alpha Ri)} + \kappa_b \end{aligned} \qquad (5.2)$$

with

$$\nu_b = 10^{-4}\ m^2 s^{-1}$$

$$\kappa_b = 10^{-5}\ m^2 s^{-1}$$

$$n = 2$$

$$\alpha = 5$$

$$\nu_0 = 5\times10^{-3}\ m^2 s^{-1}$$

Here ν_b and κ_b are the background values for respectively viscosity and diffusivity of seawater.

Peters, Gregg and Toole

A modification of the Pacanowski and Philander model was proposed by Peters, Gregg and Toole (1988). They suggest, following their measurements done in November 1984, that a better parameterization for the equatorial vertical eddy diffusivity/viscosity should be

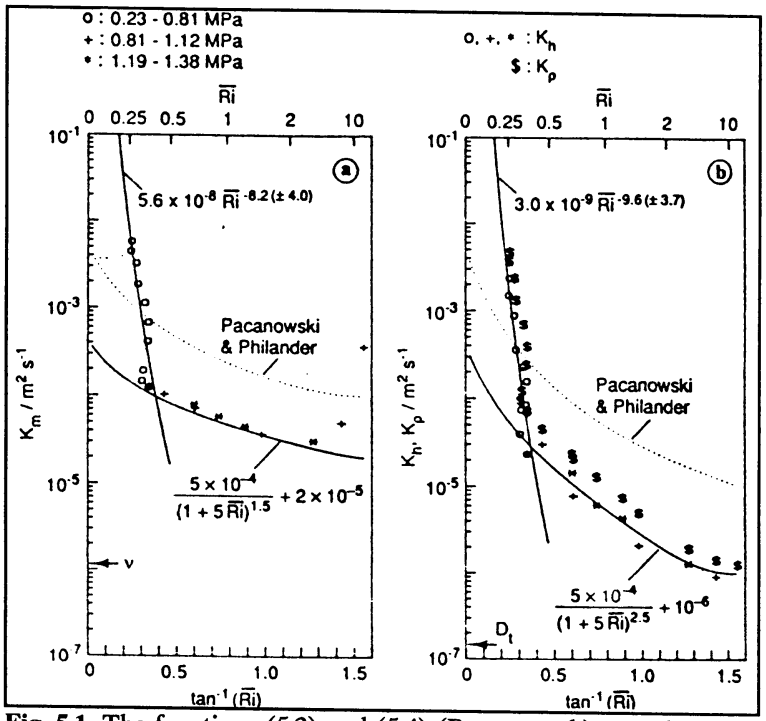

Fig. 5.1. The functions (5.3) and (5.4) (Peters et al.), together with (5.2) (Pacanowski and Philander) shown in one graph (Peters et al., 1988).

$$\begin{aligned} K_m &= 5.6\times10^{-8} Ri^{-8.2}\ m^2 s^{-1} \\ K_{T,S} &= 3.0\times10^{-9} Ri^{-9.6}\ m^2 s^{-1} \end{aligned} \qquad (5.3)$$

in the upper shear zone, 23 to 81m depth, and for the deeper part a functional form similar to that used by Pacanowski and Philander

$$K_m = \frac{5\times10^{-4}}{(1 + 5Ri)^{1.5}} + 2\times10^{-5}\ m^2s^{-1}$$
$$K_{T,s} = \frac{5\times10^{-4}}{(1 + 5Ri)^{2.5}} + 1\times10^{-6}\ m^2s^{-1} \qquad (5.4)$$

In figure 5.1 both the turbulent mixing coëfficients as expected by Pacanowski and Philander and those expected by Peters et al. are plotted against the Richardson number. The measurements of Peters et al. correspond to the dashed line (TH1) in figure 2.5.

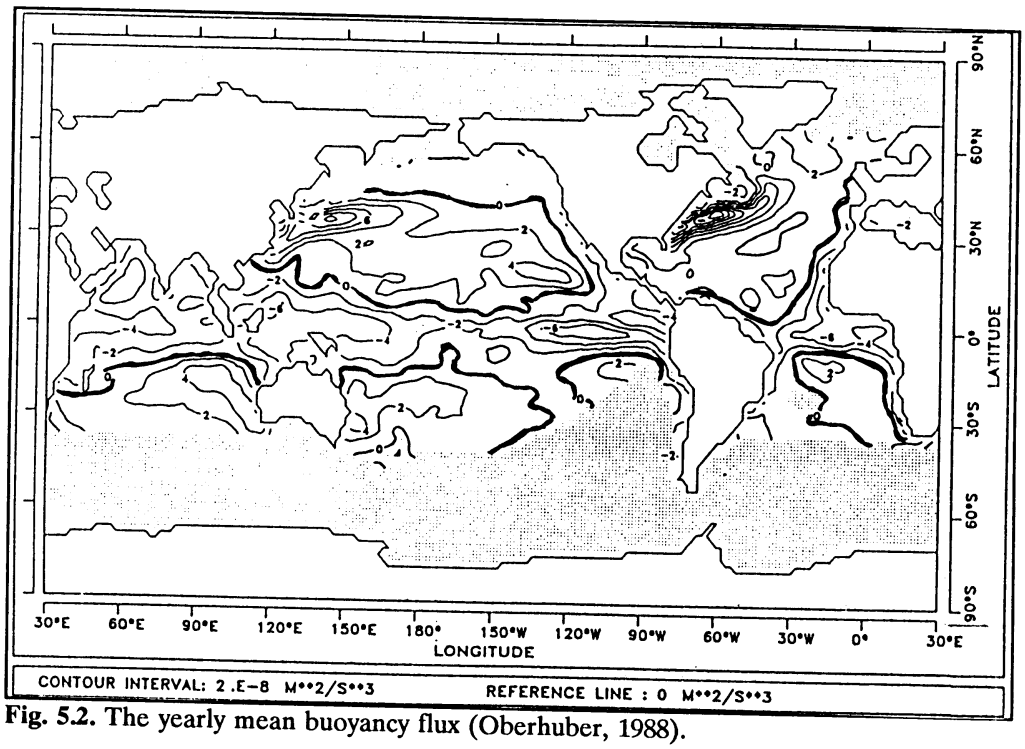

Fig. 5.2. The yearly mean buoyancy flux (Oberhuber, 1988).

5.1.2 K-profile models

In equatorial regions the buoyancy flux usually is less than zero (Fig. 5.2), so the top layer turbulence will mainly be induced by wind stress. With this in mind, assuming the mixed layer depth (h_m) to be of the same order of magnitude as the turbulent boundary layer depth (h_{obl}), some simplifications can be introduced. The assumption that h_m is equal to h_{obl} certainly doesn't hold at the equator, since at the equator below a well mixed layer a region with stratified turbulence exists. It seems however to be a reasonable assumption for the nearby off-equatorial parts of the ocean. In chapter 3 is shown that when the buoyancy flux is negative we can, following Niiler and Kraus, use equation (3.48) to calculate the depth h_m. The eddy diffusivity and eddy viscosity coefficients are computed using the following equation

$$K_M = K_{S,T} = ku_*z(1 - \frac{z}{h})^2 \qquad (5.5)$$

With k=0.4 the von Karman constant. This profile was suggested by Holtslag et al. (1991) and is used in atmospheric modelling. It is based on the assumption that the eddy viscosity/difusivity is zero at the ocean surface and at the base of the turbulent layer. The maximal value is reached when z = h/3.

The eddy diffusivity coefficient is considered to be equal to the eddy viscosity coefficient. This may be not a good assumption because some measurements at the equator indicate an eddy viscosity that is 5-10 times the eddy diffusivity (Fig. 5.3, a pressure of 1MPa corresponds to a depth of 100 m). This could be due to internal waves, which can transfer momentum without transport of heat or salinity.

Three simple parameterizations for the depth of the turbulent layer have been examined.

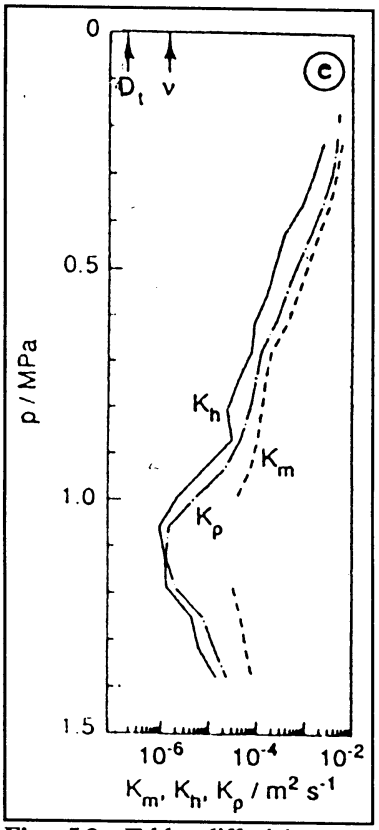

Fig. 5.3. Eddy diffusivity and viscosity profiles measured in the equatorial Pacific at 140° W (Peters et al., 1988)

The Obukhov length scale

The first of these simple models uses the generalized Obukhov length scale as a first order approximation of the depth of the turbulent ocean boundary layer. So

$$h = \frac{2u_*^3}{B_0} = L \quad . \qquad (5.6)$$

By substituting h found in equation (5.6) in equation (5.5) a parameterization for the vertical eddy diffusivity and eddy viscosity is found. Following Niiler and Kraus this stricktly is the depth of a shallowing mixed layer ($B_0 < 0$), during night or during heavy overcast conditions (3.48). When $B_0 > 0$ we consider the mixed layer depth to be $h = 4 \times 10^8 u_*^3$, which corresponds with a depth of about 50 m, when $u_* = 5 \times 10^{-3}$ ms^{-1}.

Garwood 1

Another parameterization was proposed by Garwood by introducing the length scale u_*/f, with f the Coriolis parameter (Garwood et al., 1985). This can also be interpreted as introducing an extra dissipation term hfu_*^2 in equation (3.43). The turbulent layer is now computed with

$$h = \frac{1}{\frac{1}{L} + \frac{1}{u_*/f}} \qquad (5.7)$$

Note that when L becomes very large $h \approx u_*/f$.

Garwood 2

For a more analytical way to introduce such a Coriolis parameter dependent scale we have to go back to equation (3.20), the turbulence kinetic energy equation. When we split up this equation in three directions and define $e_\beta = 1/2 \langle u_\beta'^2 \rangle$ with the condition that we do not sum over β (!) we find that the Coriolis force dependent parameter in Eq. (3.9) doesn't dissappear. Equation (3.20) yields

$$\frac{De_\beta}{Dt} + 2\epsilon_{\beta jk}\Omega_j \overline{u_\beta' u_k'} = -\overline{u_\beta' u_j'}\frac{\partial \bar{u}_\beta}{\partial x_j} + \frac{\overline{u_\beta' p'}}{\rho_0} -$$
$$\frac{\partial}{\partial x_j}\left(e_\beta' u_j' + \frac{1}{\rho_0}\overline{p' u_\beta'}\delta_{\beta j} + \nu\frac{\partial e_\beta}{\partial x_j}\right) + \frac{1}{\rho_0}\overline{p'\frac{\partial u_\beta'}{\partial x_\beta}} - \nu\overline{\left(\frac{\partial u_\beta'}{\partial x_j}\right)^2}. \qquad (5.8)$$

in which the penultimate right hand side term is new as well. This is the so called "return to isotropy" term that distributes the TKE over the three directions. Eq. (3.20) is nothing but Eq. (5.8) summed over the three directions. With the assumptions of horizontal homogeneity and stationarity and analogous to the derivation of (3.46) we find, similar to (5.7), the depthscale

$$h = \frac{C_1 L}{1 + C_2 \Phi}, \qquad (5.9)$$

with

$$\Phi = \frac{\Omega_y \tau_x}{\rho B_0} \qquad (5.10)$$

For the constants C_1 and C_2 we choose, following Garwood and Muller; $C_1 = 1$ and $C_2 = 12/7$.

5.2 An integral mixing model

Integral models make use of the assumption that a well mixed layer exists. By local energy considerations the depth of this layer is determined.

Kattenberg

A model developed by Kattenberg (personal communication), a Niiler-Kraus type of mixing scheme, is also implemented. It is based on a local vertical budget for turbulent kinetic energy as given by equation (3.43). With the neglection of the energy due to internal waves(!) and neglecting the penetration of solar radiation this equation is written as follows

$$\Delta E_{pot} + \Delta E_{kin} + mu_*^3 - \int_{-h}^{0} \epsilon dx_3 = 0 \qquad (5.11)$$

where ΔE_{pot} and ΔE_{kin} represent the changes in potential and kinetic energy in the water column due to mixing processes. The mixed layer system is solved with a method of succesive approximation. I.e. the algorithm calculates properties of a mixed layer of a given depth and the turbulence kinetic energy budget according to equation (5.11). This is done for succesively deeper approximations of the mixed layer depth. If too small or too high values for h are chosen, the budget (5.11) will not balance. The algorithm increases the mixing depth, until a depth is reached at which the TKE budget does balance. Such a simple stepping technique can be used because we are dealing with a rather coarse vertical grid of an OGCM. (Not many steps have to be made to reach the best possible approximation for the mixed layer depth.) Usually the mixed layer depth will fall between two succesive computation layers. In this case there remains a portion TKE after mixing the first n layers, that is not enough to mix in the (n+1)-th layer as well. This (n+1)-th layer then is mixed partially with the mixed layer above. The part of the new layer that is mixed in is determined by the TKE that is available. The dissipation ϵ is considered to have an exponential decay with depth of $\exp(z/z_L)$ with $z_L = 0.4(u_*/f)$.

6 Results

In this chapter we show the effects of the various mixing schemes on the behaviour of the OGCM. We treat them in the same order as in chapter 5. For convenience only the fields of the month September are shown in this chapter (unless otherwise stated). In chapter 7 we take a closer look at the seasonal cycle.

6.1 The quality of an OGCM

In order to have the possibility to make some qualitative statements with respect to an OGCM, we consider the prescribed COADS heat and salt fluxes and the Hellerman and Rosenstein momentum fluxes to be the "real" climatology (see chapter 4). Similarly we take the mean monthly SST's as given by COADS for the real mean SST's, for the month that is considered. An ideal OGCM would give a heat flux error that is equal to zero, i.e. an ideal OGCM, when forced with the COADS fluxes, would produce the COADS SST's. So with the assumption that there are no errors in the above mentioned data sets we can use the heat flux error as a measure of the quality of an OGCM.

Another measure for the quality of an OGCM could be chosen its ability to simulate a realistic equatorial undercurrent. It is however not easy to define the properties of a realistic undercurrent because it is highly variable (Fig. 2.5) and not enough observations are available to define a climatology. For our purpose a realistic equatorial undercurrent is defined as one that has a velocity maximum of about 1.0 ($\pm$ 0.4) ms^{-1} at a depth of 100 ($\pm$ 20) m at 140° West. Above the equatorial undercurrent we expect to find a linear velocity profile from the surface to the core, as found by measurements. Another observed feature of the equatorial undercurrent is that the speed at 25m depth at 140° West has a seasonal variation (Fig. 2.5).

As a third measure for the quality of an OGCM we choose its ability to simulate a well developed warm pool (Fig. 1.4). This warm pool seems to be very important in the El Niño mechanism. There are however no reliable measurements concerning the seasonal change and a climatological depth of the warm pool.

6.2 Common problems

The model experiments have been performed in such a way that they are in agreement with the demands of the TOGA-NEG intercomparison. Seven groups have submitted results to the ocean model intercomparison, and as mentioned before (see 1.3) some common problems arise in simulating the Pacific (WCRP, personal communication):

i) all models simulate too cold sea surface temperatures along the equator;
ii) temperatures are too high along the south American coast and 110°W 5°N;
iii) the warm pool in the western Pacific is not as deep as the observed warm pool.

Also can be said that not all models are able too simulate an undercurrent with a realistic speed. Figure 6.1(a) shows the temperature errors of the Max Planck Institut (MPI). Figure 1(b) of Oxford and figure 1(c) of the KNMI model for the month September. (Note the contour interval is 0.5° for the Oxford and MPI model and 1.0° for

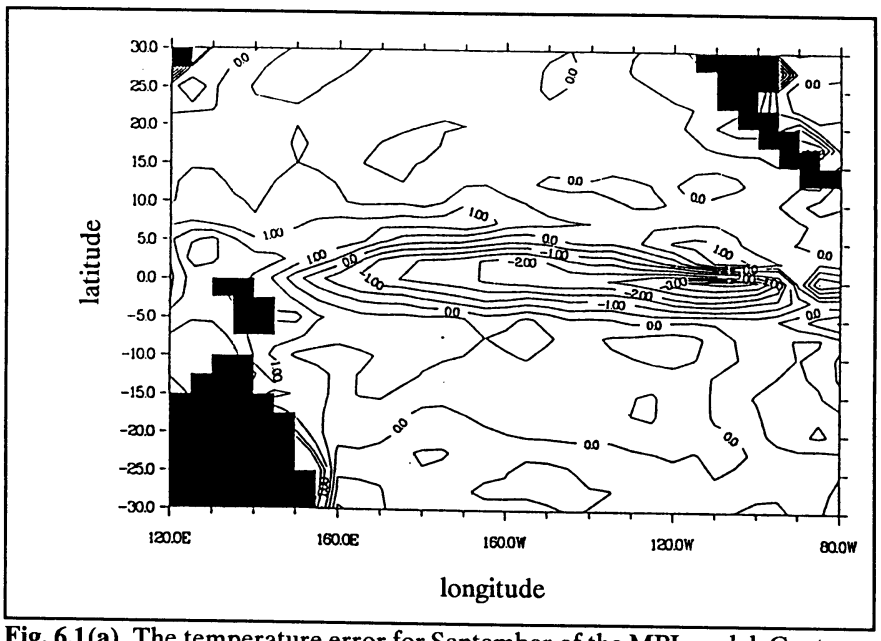

Fig. 6.1(a). The temperature error for September of the MPI model. Contours are 0.5°C (TOGA-NEG, 1991).

the KNMI model). The vertical mixing scheme used in these models is in all cases that as proposed by Pacanowski and Philander (Eq. 5.2). All three models have too low SST's along the equator and too warm temperatures around 110°W, 5°N. These temperature errors correspond to heat errors that are as big as or even greater than the total incoming net heat flux (see appendix). Figure 6.2 shows the modelled 26°C isotherm in the Western Pacific of the Oxford model (210°E corresponds to 170°W). We show the isotherm in March because the measurements shown in figure 1.5 are from the same period (Lemason et Piton, 1968). The modelled 26°C isotherm doesn't get below 100 m depth. Figure 1.5 shows an observed 26°C isotherm at a depth of about 140 m. The 26°C isotherm measured by Lemason and Piton is deeper than all models compute. The measurements are however not very reliable because they were measured during two months from east to west, while a light El Niño event took place.

6.3 The various mixing schemes

The goal of this research is to examine how the choice of a certain mixing scheme influences the quality - as defined above - of an OGCM. In order to do so we tried all the mixing schemes described in chapter 5 and looked at the characteristics of a certain mixing scheme with respect to the difficulties described in 6.2. We judge instantaneous fields by eye. To make plausible, that for this purpose this is a good procedure figures 6.3(a) and 6.3(b) show two instantaneous fields and the corresponding monthly averaged fields. The distinctions due to differences in mixing parameterization are much larger than those due to averaging. The same applies to the fields of the vertical velocity and the vertical temperature structure (not shown). Fields that aren't important for the argumentation are not shown.

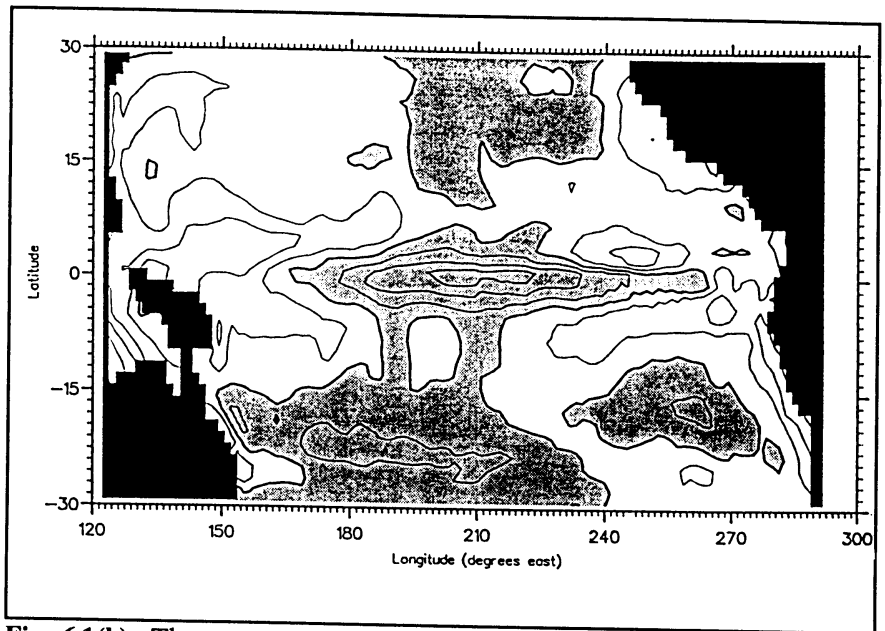

Fig. 6.1(b). The temperature error in September for the Oxford model. Contours 0.5°C, the shaded region corresponds to negative errors (TOGA-NEG, 1991).

6.3.1 No mixing scheme (NM-case)

The first thing that seems convenient when inquiring the influence of a certain parameterization of vertical mixing is to look what goes wrong when you don't parameterize vertical mixing. This is exactly what is done here. We take the fields of the Pacanowski and Philander (PP) parameterization as a reference. This because most OGCM's use this parameterization. The vertical equatorial zonal velocity structure of the PP-case is presented in figure 6.4 (above); the heat error for the PP-case is presented in figure 6.3(a); the equatorial temperature structure in figure 6.5 (above).

The equatorial undercurrent (EUC)

In figure 6.4 the equatorial zonal velocity of the NM-case is compared with the PP-case. (With the PP-case is meant the GCM with an Pacanowski and Philander parameterization of vertical turbulent mixing, etc.). The whole linear (stable) profile turns into a highly instable profile in the top 100 m (Rayleighs bendpoint criterium, see 2.1) with two maxima at 140°W. This instable situation needs adjustment (which is exactly what the PP-scheme is for). The westward momentum, because of the absence of turbulent mixing, isn't transported downward sufficiently (see also Wacongne, 1989). So vertical mixing is needed to simulate the EUC properly.

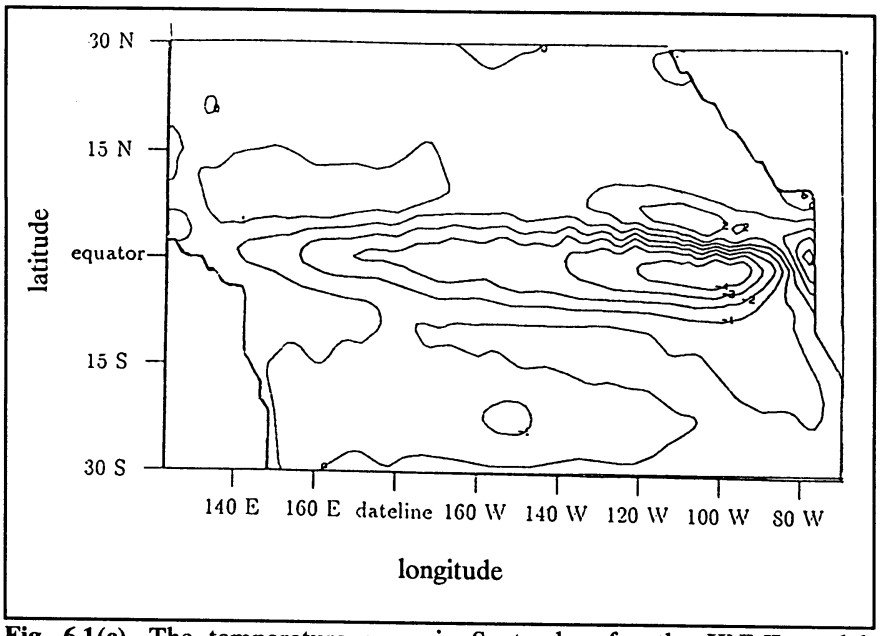

Fig. 6.1(c). The temperature error in September for the KNMI model. Contourinterval 1.0°C.

The heat error

However the maximum heat error is very large and varies from about 80 Wm^{-2} in December to 140 Wm^{-2} in September, it even improves when compared with the heat error of the PP-parameterization. The positive heat error at the equator corresponds with too cold surface temperatures. Not much is happening with respect to the hot spot at 110°W, 5°N (not shown).

The warm pool

The warm pool is similar to that of the PP-case (Fig. 6.5 (above)). However in December and March this warm pool is deeper (not shown). More about these seasonal differences in chapter 7.

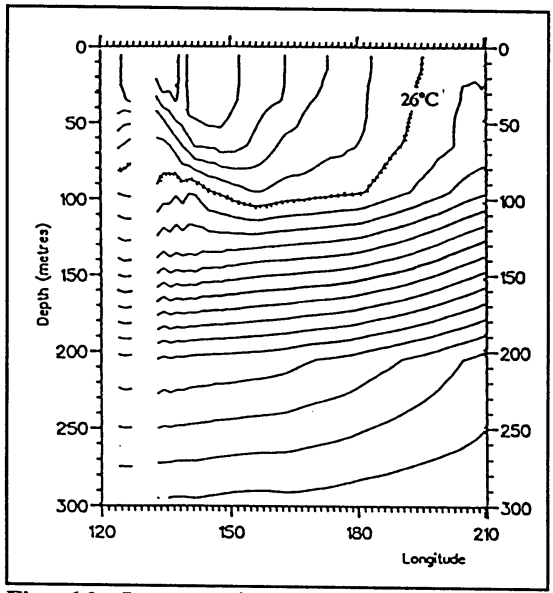

Fig. 6.2. Isoterms in the western Pacific in March computed by the Oxford model. Contours are 1°C (TOGA-NEG intercomparison, 1991).

6.3.2 Differential mixing schemes

Pacanowski and Philander (PP)

The most often used mixing scheme in GCM's of the equatorial ocean is that proposed by Pacanowski and Philander (Eq. 4.2).

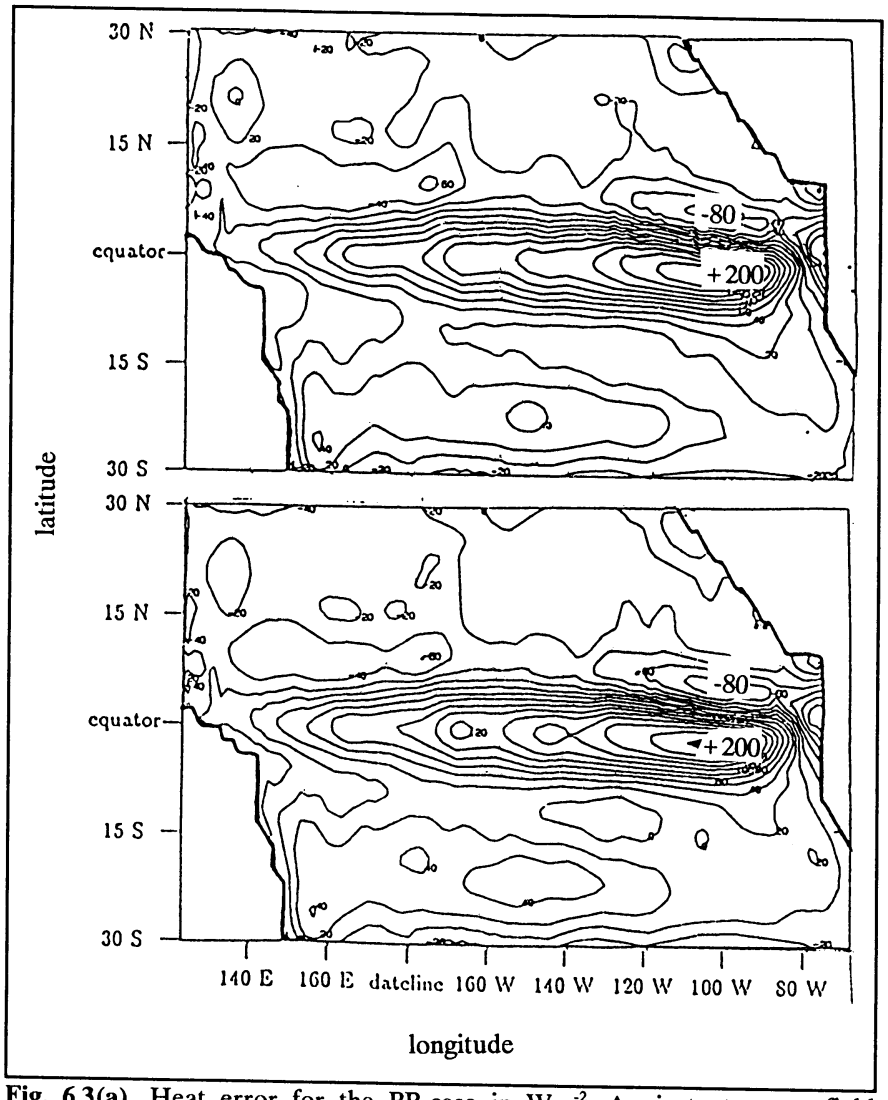

Fig. 6.3(a). Heat error for the PP-case in Wm^{-2}. An instantaneous field (above) is compared with a monthly mean field (below).

The EUC

As mentioned before a Richardson number dependent mixing scheme has advantages. The velocity maximum of the equatorial undercurrent lies at a reasonable place, with a linear velocity profile from the surface to the core of the undercurrent (Fig. 6.4 (above)). The maximum velocities, especially for the months June and September, however seem too slow. So with a Richardson number dependent parameterization of vertical mixing we improve the vertical velocity structure with respect to the OGCM without a parameterization for vertical mixing. Note that both the eastward and the westward velocity maxima are lower in the PP-case compared to the no-mixing case (Fig. 6.4). The velocity structure is "pulled straight" by Ri-number dependent mixing.

The heat error

As mentioned before the maximum heat flux errors are even bigger than those computed

with an OGCM without a mixing scheme and are about 80 Wm^{-2} for the months March and December, 140 Wm^{-2} for June and even more than 200 Wm^{-2} in September. These values are bigger than the net inward heat fluxes.

The warm pool

Just like in the no mixing case, the warm pool is not very deep (Fig. 6.5).

Remark

The Pacanowski and Philander parameterization behaves similar to the much simpler approach in which we set the eddy diffusivity coefficient K equal too 10^{-3} m^2s^{-1} if $Ri < Ri_{cr}$ and $K = \nu$ for $Ri > Ri_{cr}$. Where ν is respectively the molecular viscosity or diffusivity. We chose $Ri_{cr} = 0.5$. This parameterization has almost the same features as the Pacanowski and Philander parameterization. So for reasons of simplicity an computational economy it seems preferable to use a scheme like this.

Peters, Gregg and Toole (PGT)

This scheme is a modification of the Pacanowski and Philander mixing scheme (Eqs 5.3 and 5.4). It is a fit to measurements as done by Peters, Gregg and Toole (1988). This parameterization is mentioned in this study because this scheme was originally implemented in this OGCM.

The EUC

The same as for the PP-case, which may seem surprising because the diffusivity/viscosity coefficients are up to ten times greater. It is however to be expected because one cannot make a profile straighter than straight.

The heat error

It yields the same results as the Pacanowski and Philander scheme.

The warm pool

Also the same as for the PP-case (not shown). The Peters et al. scheme doesn't seem fruitful in an OGCM, maybe it is however a more convenient parameterization in high resolution models.

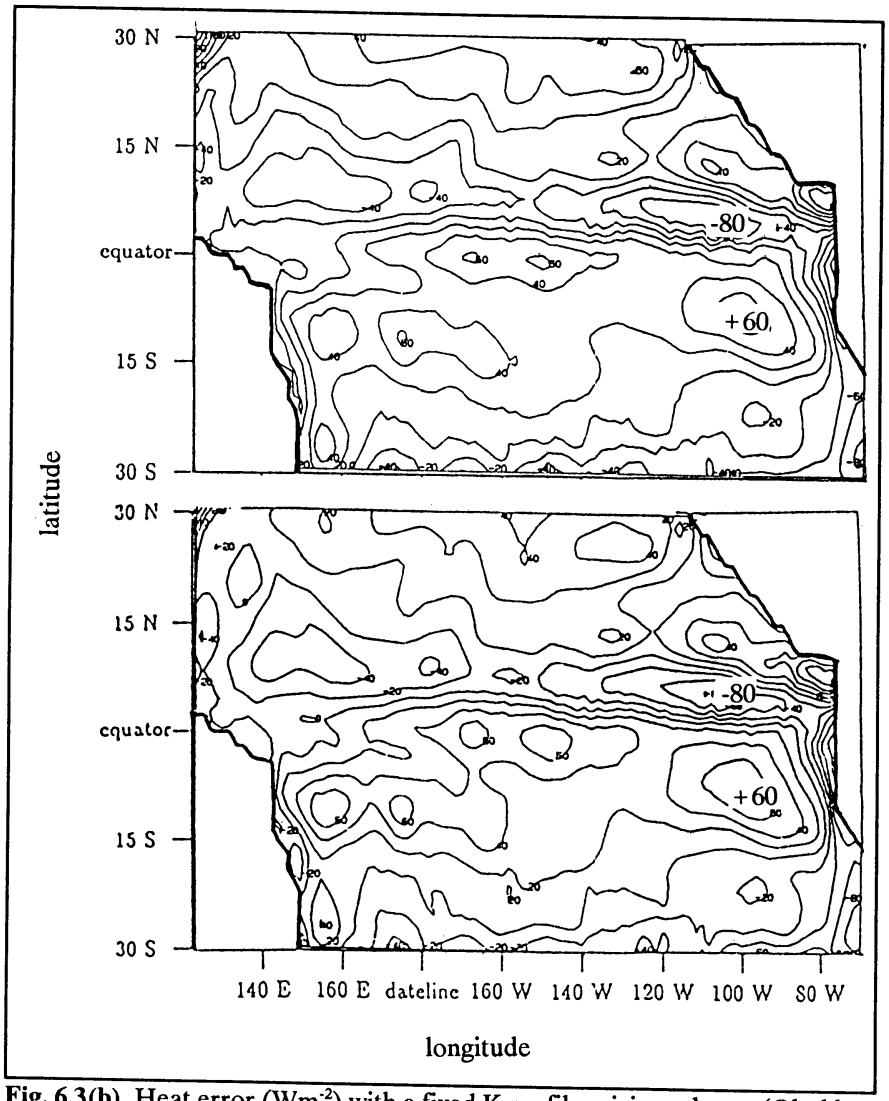

Fig. 6.3(b). Heat error (Wm^{-2}) with a fixed K profile mixing scheme (Obukhov length). The instanteneous field (above) compared with the monthly mean field.

The Obukhov length scale (OB)

The EUC

The vertical velocity structure in the upper 75 m is as instable as without mixing (Fig. 6.6 (above)). The velocity maximum is however significantly lower. In contrary to the previous cases the water begins to speed up at the east of 160°W. This points out to a change in the zonal pressure gradient/ westward momentum balance (Wacongne, 1989). There is the great difference in the velocity of the undercurrent between the months June and September (strong westward winds) on one side and the months December and March on the other side.

The heat error

The model is improved with respect to the heatflux error at the equator (Fig. 6.3(b)),

when compared with the PP- and NM-case. For March and December the error at the equator is approaching the 30 Wm^{-2} and, except for the region 110°W, 5°N, in June and September the error decreases by more than a factor two.

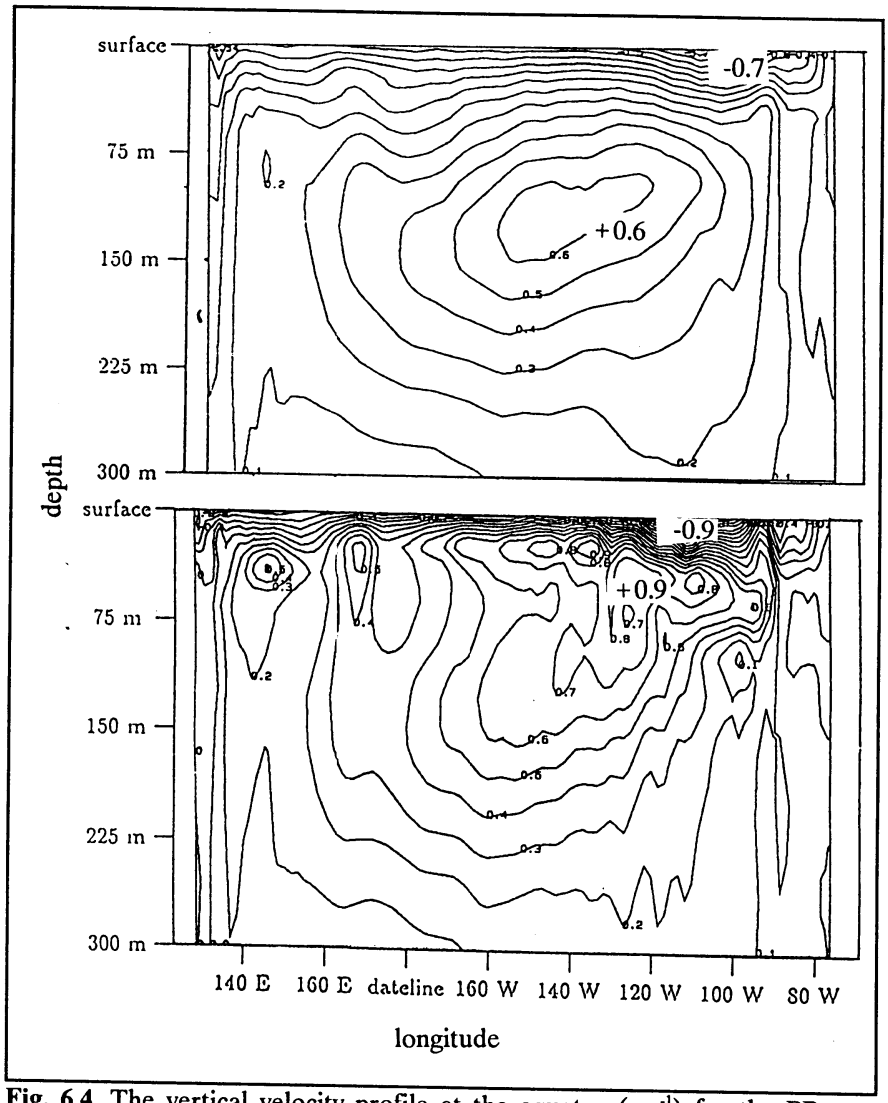

Fig. 6.4. The vertical velocity profile at the equator (ms^{-1}) for the PP-case (above) and the NM-case (below).

The warm pool

The warm pool in the west is much deeper than in the previous cases (Fig. 6.5 (below)). The thermocline however is not very sharp in the eastern Pacific. Note that in the upper 150 m the temperature is constant for one depth at the west of 160° W

Garwood 1 (G1)

The fields produced by the OGCM with a mixing scheme described by (5.5) and (5.7), have mainly the same features as the fields produced by the parameterization with the Obukhov length scale. This is not surprising because at the equator these two models should be the same. We can write (5.7) as

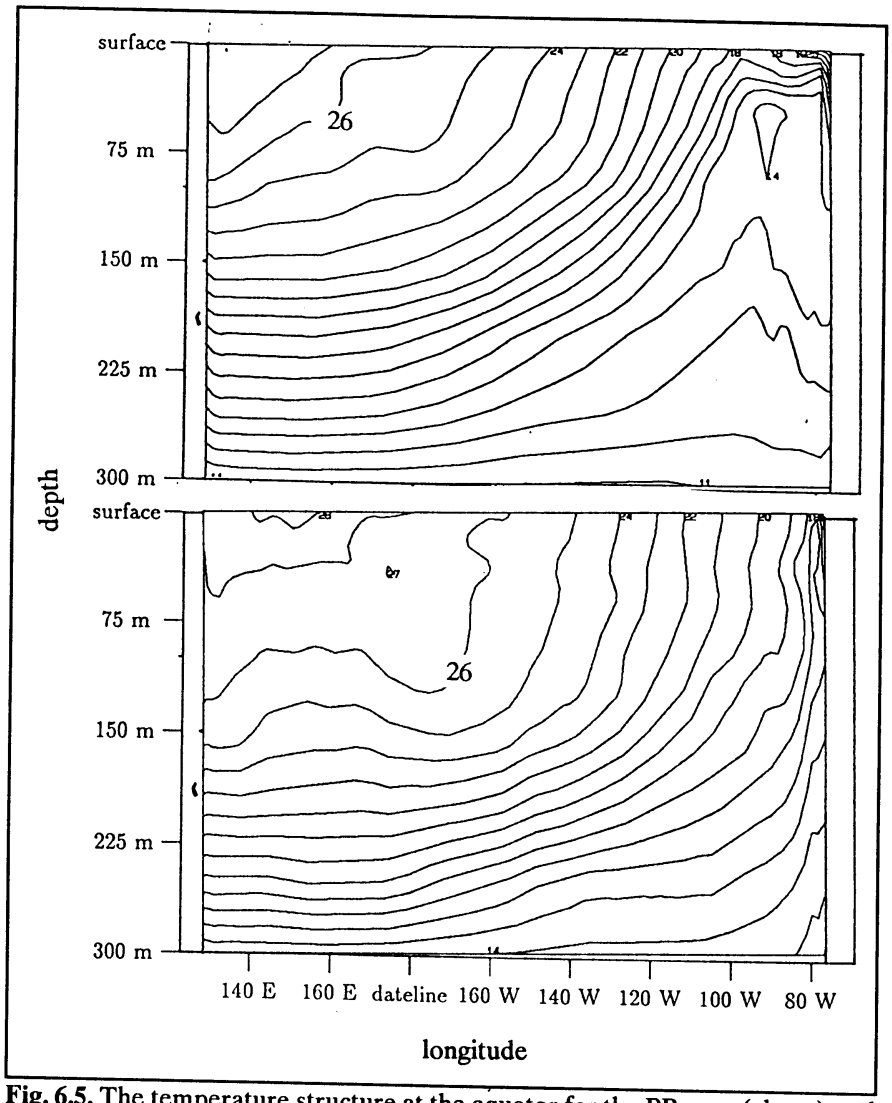

Fig. 6.5. The temperature structure at the equator for the PP-case (above) and the OB-case (below), contours are 1°C.

$$h = \frac{L}{1 + \frac{Lf}{u_*}} \qquad (6.1)$$

It is clear that h ≤ L, and near the equator h will only be slightly less than L.

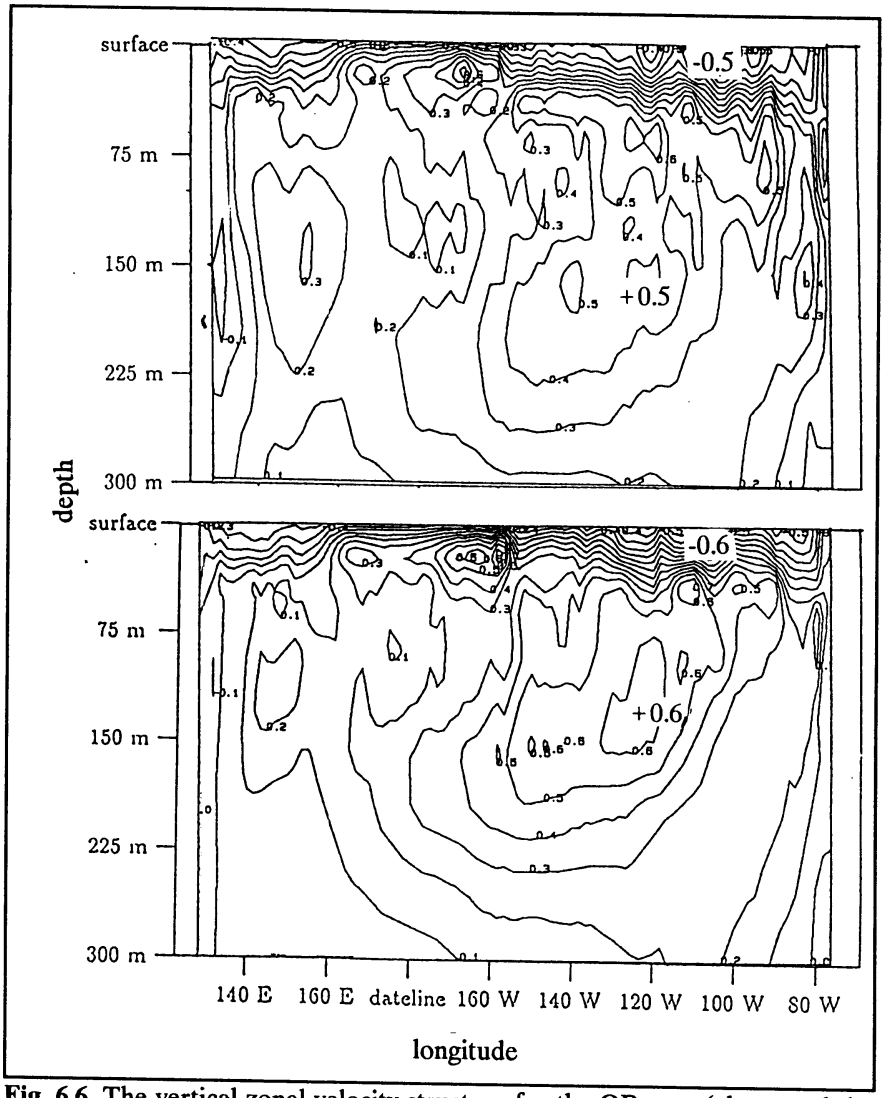

Fig. 6.6. The vertical zonal velocity structure for the OB-case (above and the G2-case (below), contours 1 ms^{-1}.

Garwood 2 (G2)

The EUC

The velocity structure has very much the same features as the previous two cases. The undercurrent is however faster and seems somewhat less instable (Fig. 6.6 (below)). The discontinuity in the upper 150 m at 160°W, which seems to be directly connected with a well developed warm pool (Fig. 6.7).

The heat error

The heat error is approximately the same as in the previous two cases. There may be a little improvement for the months March and December when winds are low (not shown).

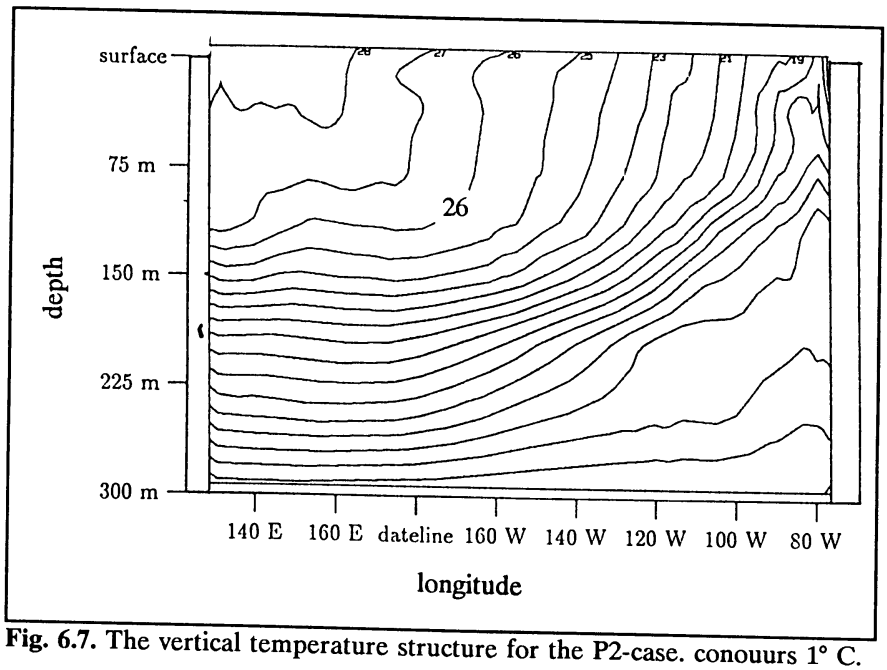

Fig. 6.7. The vertical temperature structure for the P2-case. conouurs 1° C.

The warm pool

The warm pool is well developed. The thermocline is sharper when compared with the previous two cases (Fig. 6.7).

Remark

With respect to th PP-case the previous three parameterizations improve the heat error in the cold tongue remarkably. The hot spot is not much affected. Also the warm pool is much better developed. The equatorial velocity profile however becomes instable and the thermocline weakens. The Garwood 2 seems to have the best performance.

6.3.3 An integral mixing scheme

Kattenberg

The EUC

The velocity structure is different with respect to the previous cases (Fig. 6.8(a)). More specifically we can say that the velocity maximum lies too deep. Most mixing is in the eastern Pacific, where very much eastward momentum is dissipated. This seems to cause the convergence at about 170°E. Due to this we expect a deep warm pool.

The heat error

For a great area between 10°N and 10°S the heatflux error improves remarkably (Fig. 6.8(b)). Moreover the whole temperature structure changes. (The heat error at 0°N, 120°W is 140 Wm^{-2} in the no-mixing case and about 0 Wm^{-2} with the Kraus-Turner mixing scheme.) Also the hot spot warms (so there is much (too much?) off-equatorial mixing, see section 7.1)

The warm pool

Figure 6.8 (c) shows a very deep warm pool in the western Pacific but no sharp thermocline in the eastern Pacific (see Fig. 1.4). A relation between (by mixing) destructed eastward momentum in the eastern Pacific and the depth of the warm pool seems to exist!

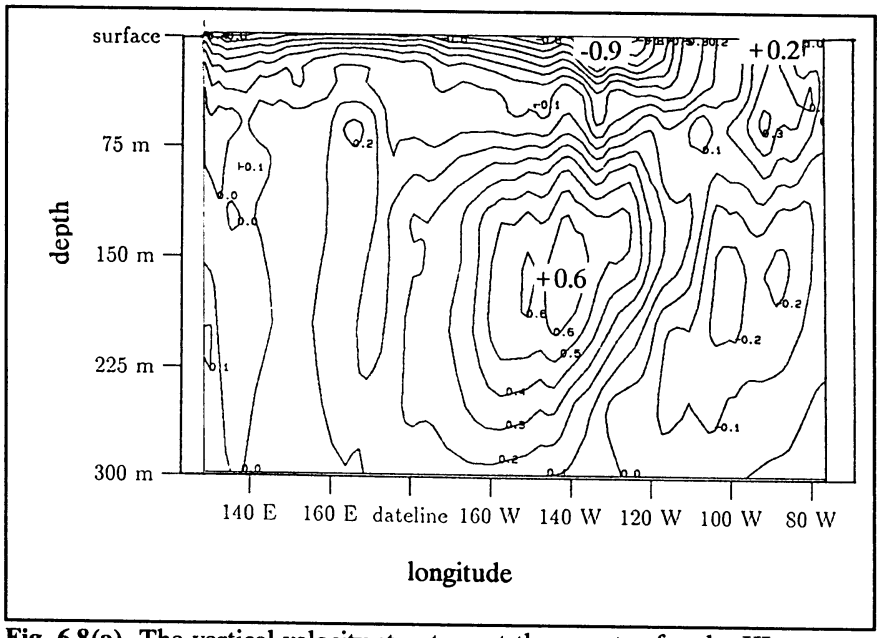

Fig. 6.8(a). The vertical velocity structure at the equator for the KI-case.

6.4 Combinations

So far we can conclude that a PP-scheme improves the performance of the OGCM with respect to the velocity structure, and that a fixed K-profile scheme improves the performance with respect of the cold tongue and the warm pool. A combination of these two approaches suggests itself. This notion is legalized by the fact that Ri-number dependent parameterizations are based on measurements of 20 meters and deeper (Gregg et al., 1985).

In the Appendix are the fields shown of a model with between 10°N and 10°S a surface mixed layer with the G2-depth scale (Eqs. 5.9 and 5.10); outside 10°N and 10°S a layer of 50 m depth with a vertical eddy diffusivity of 10 $^{-3}m^2s^{-1}$ was defined. Below the surface layer the PP-scheme was employed. The horizontal diffusivity/viscosity was chosen to be 3000 m^2s^{-1}.

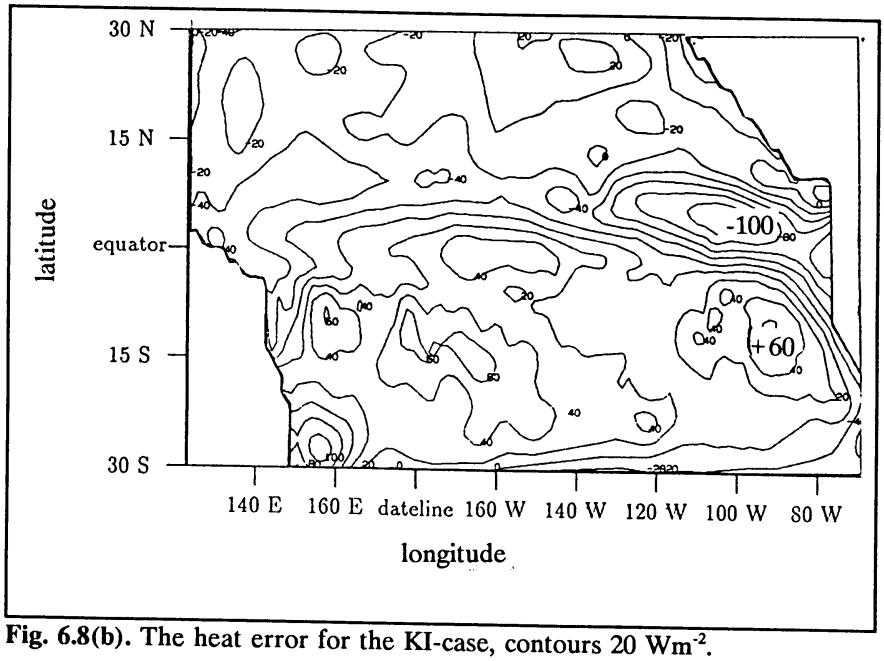

Fig. 6.8(b). The heat error for the KI-case, contours 20 Wm^{-2}.

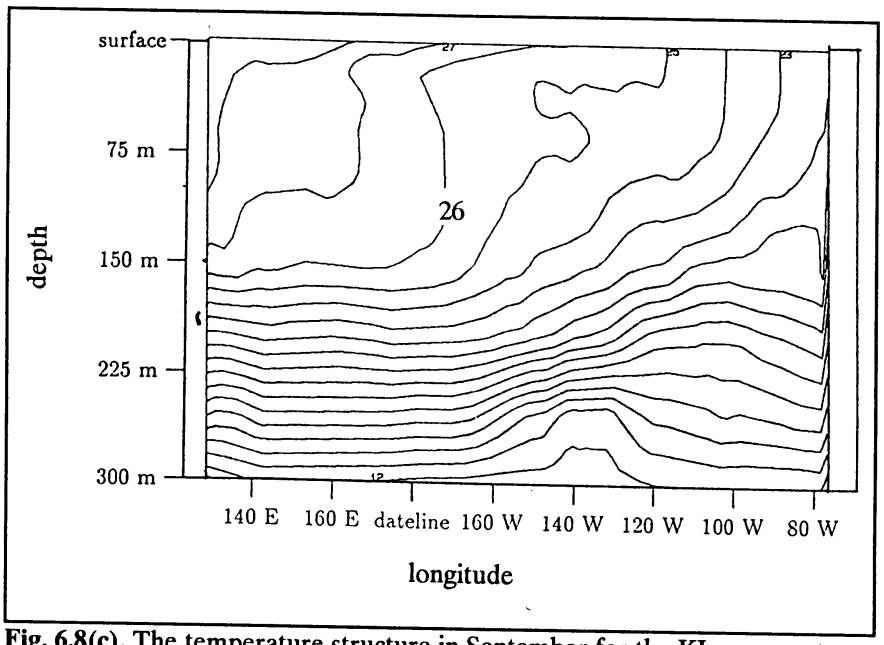

Fig. 6.8(c). The temperature structure in September for the KI case, contours are 1° C.

7 Interpretation

Here the results of chapter 6 will be discussed and interpreted in the light of supplementary experiments. The problems in ocean modelling as mentioned in section 6.2 will be considered. Also some remarks will be made with respect to the heat storage mechanism in the warm pool.

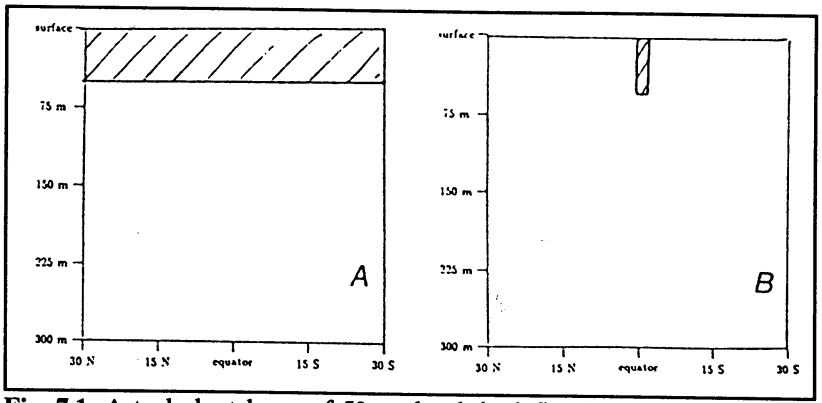

Fig. 7.1. A turbulent layer of 50 m depth is defined A: everywhere and B: only between ± 1°.

7.1 The heat error at the cold tongue

Like in most models of the equatorial Pacific the sea surface temperatures in the central and eastern equatorial region tend to be several degrees too cold. As already shown in chapter 6, surface mixing reduces this temperature error (heat error). A great difference, between models that use surface fluxes dependent parameterizations (u_*, B_0) and models that use Richardson number dependent parameterizations for vertical mixing, exists especially in the months June and September, when easterly winds are high over the whole Pacific (Fig. 7.10). What are the reasons for these differences?

As mentioned before, (patchy) turbulence generated by shear stress only arises when the Richardson number is small (Ri $\approx$ 0.25). In the equatorial Pacific model the Richardson number gets only small enough at the equator, i.e. where the equatorial undercurrent flows. So a Richardson number dependent mixing scheme will only affect the equatorial region. Hence one can suggest that the great difference in heat error between the above mentioned approaches is due to off-equatorial mixing.

To strengthen this argument we consider the following two cases. Figure 7.2(a) shows the heat error in September for the OGCM with a 50 m deep surface layer (the 2 highest computation layers). The eddy viscosity/diffusivity in the layer is K = 10^{-3} m^2s^{-1}. Fig 7.2(b) shows the case where only at the equator, between 1°N and 1°S there is a 50 m deep surface mixed layer. These cases are schematically shown in figure 7.1. In both cases the heat error is reduced when compared with the no-mixing case. Both off-equatorial and equatorial mixing seem to be important.

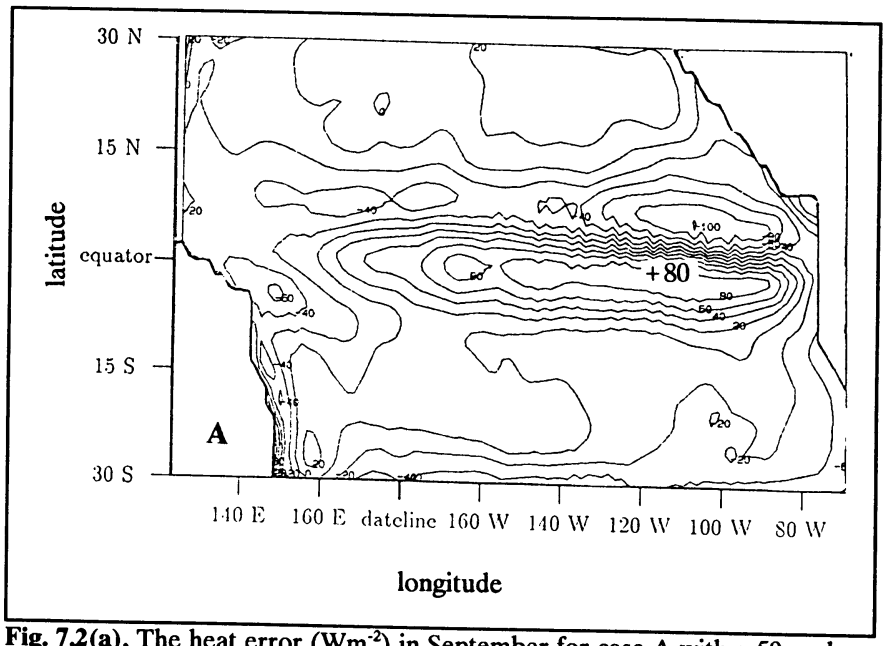

Fig. 7.2(a). The heat error (Wm^{-2}) in September for case A with a 50 m deep turbulent layer ($K_{S,T,M} = 10^{-3}\ m^2s^{-1}$).

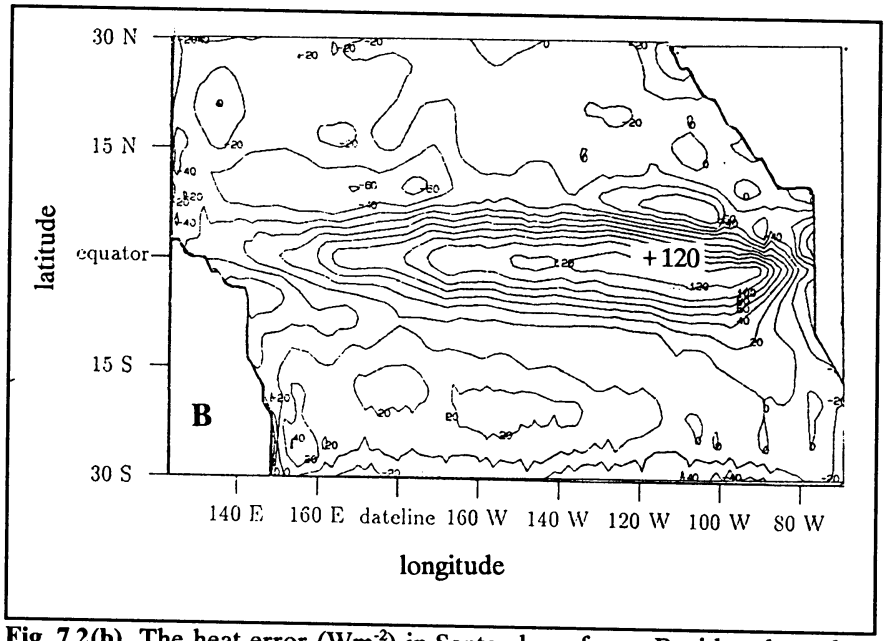

Fig. 7.2(b). The heat error (Wm^{-2}) in September of case B with only surface mixing at the equator.

The exact location of off-equatorial mixing is less important, as demonstrated by the following experiment. Consider the next four cases: the PP-case (see chapter 6) without surface mixing, marked with number 1; three other cases, called case 2, 3 and 4, also with a PP-mixing scheme but with a regional (region 2,3 or 4, in Fig. 7.3(a)) turbulent layer with a depth of the Obukhov length (~ 100 m). These regions with surface mixing are shown in figure 7.3(a). Figure 7.3(b) shows the 26°C isotherms the equator of these four models. The whole equatorial slice is warming due to off-equatorial mixing.

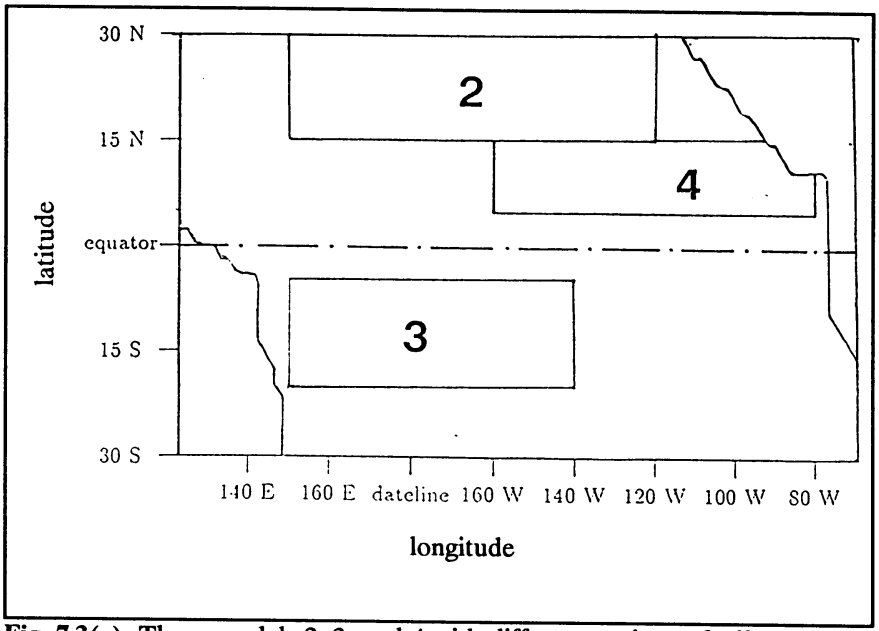

Fig. 7.3(a). Three models 2, 3, and 4 with different regions of off-equatorial mixing.

Mixing in the surface layers at the equator does have an effect on the upwelling and meridional circulation there. Figure 7.4 shows two cross-sections at 140°W with the vertical upward velocities in meters per day of the NM -case and of case *A* of the experiment described in section 7.1 (see Fig. 7.1). Without surface mixing there is an upwelling of 4 meters/day; with surface mixing this speed is 2 meters/day. Without surface mixing the maximum upward speed is also closer to the surface than with surface mixing.

Thesis

Surface mixing can reduce the heat error at the cold tongue in at least two ways:

1. By turbulence heat is transferred more effectively from the atmosphere to the ocean. Due to off-equatorial mixing the subsurface ocean layer becomes warmer.
2. Equatorial mixing tends to suppress the upwelling of water at the equator. The upwelled water at the equator is therefore drawn from another depth. A circulation cell develops under influence of surface mixing.

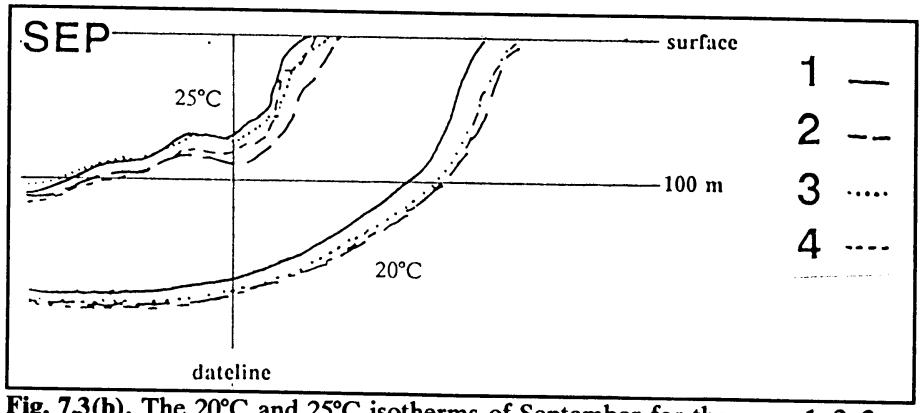

Fig. 7.3(b). The 20°C and 25°C isotherms of September for the cases 1, 2, 3 and 4.

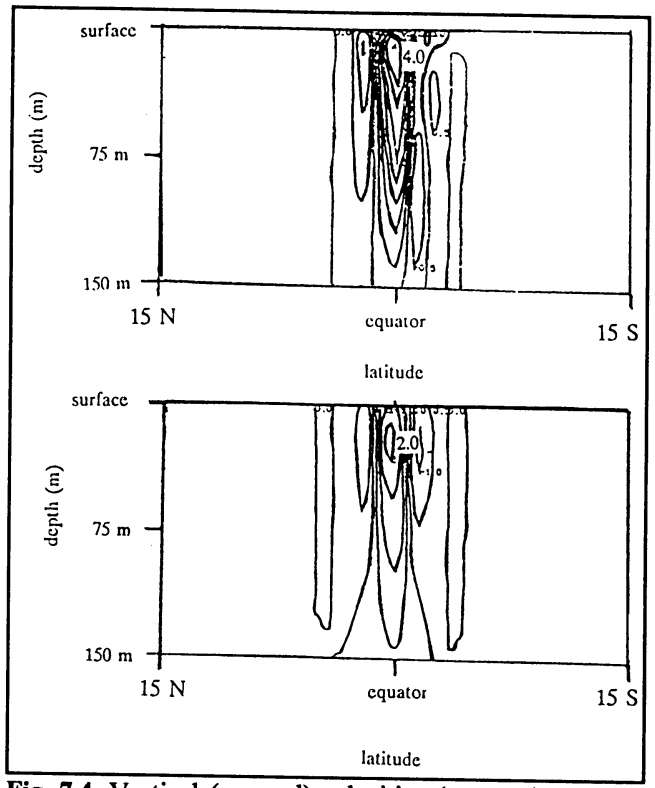

Fig. 7.4. Vertical (upward) velocities (meters/day) with out surface mixing (above) and with surface mixing (below).

7.2 The hot spot at 110W, 5N

Mixing does not have a great influence on the strength or the place of the hot spot at 110°W, 5°N. Fig. 7.5(b) shows that strong downwelling exists to the south of the spot. The mean lateral flow is northward. This downwelling lies at a latitude at which we would

expect the north equatorial countercurrent (NECC). This current is related to the convergence of the intertropical convergence zone (ITCZ), (Gill,1982). This ITCZ is not represented very well in the model because the resolution of the wind data is not fine enough. We think that the convergent air motion of the ITCZ, and the associated divergent seawater motion, in reality is strong enough to suppres this downwelling cell. Hence: we think that this spot can only be dealt with by using a greater resolution in both the model and the windstress data. So:

Thesis

The hot spot at 110° W, 5° N is a resolution problem. The ITCZ is not well represented in the wind data.

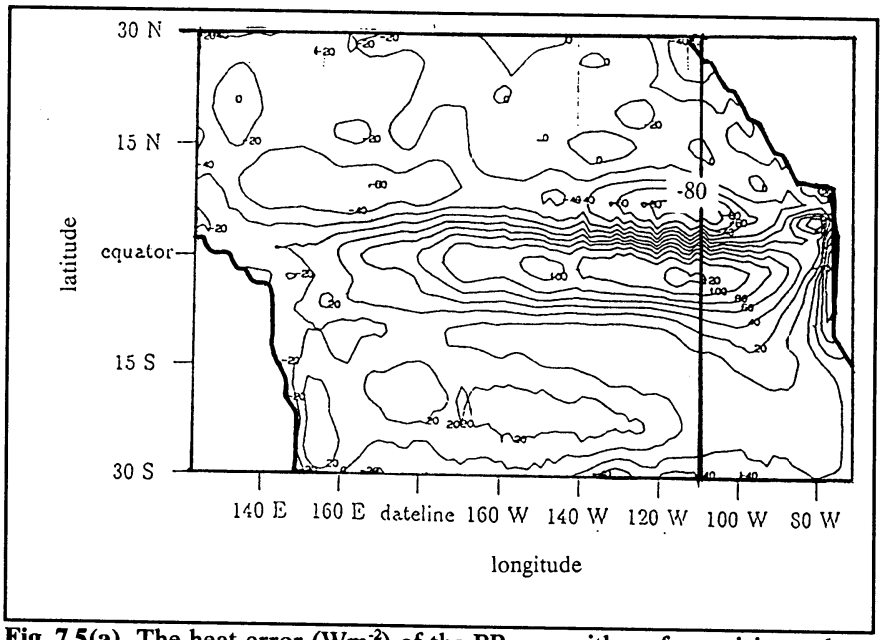

Fig. 7.5(a). The heat error (Wm^{-2}) of the PP-case with surface mixing only at the equator (see section 7.4).

7.3 The equatorial undercurrent

Equatorial subsurface mixing is very important to provide the linear velocity profile from the surface to the core of the EUC (Fig. 6.4). The best method to do this is by using the nonlinear parameterization as proposed by Pacanowski and Philander or another Richardson number dependent parameterization. Surface mixing also affects the zonal momentum balance (compare Fig. 6.4 with Fig. 6.6). With surface mixing the EUC at a depth of ~100 m starts speeding up first at the east of the dateline (Fig. 6.6). Without surface mixing the EUC speeds up already near the New Guinean coast (Fig. 6.4).

The absolute speed of the EUC is merely fixed by the horizontal diffusion (see chapter 4) as shown in figure 7.6, which shows the PP-case with various values for the horizontal diffusion coefficient. Only contours of eastward speed > 0.5 ms^{-1} and westward speed < 0 ms^{-1} (hatched) are shown.

Also a biharmonical parameterization was tried but it turned out to have the same performance as the harmonical parameterization with a low horizontal diffusion. Maybe the resolution of this model is not high enough to profit from a biharmonical parameterization.

The westward current in March at the west of the dateline is a curiosity of our KNMI-model (see also Appendix). Other models don't get the current. There is however some evidence that this westward flow also appears in realitys. Figure 7.7 shows some measurements in the Western warm pool of February 1990, (Brainerd and Gregg, 1991). In this picture a pressure of 1 Mpa corresponds to a depth of 100 m. Although the measurements are relative to the ships' motion definately a minimum in eastward speed under the surface exists. Maybe this westward flow is part of a closed circulation in the western warm pool which could be an important link in the build up and conservation of the warm pool!

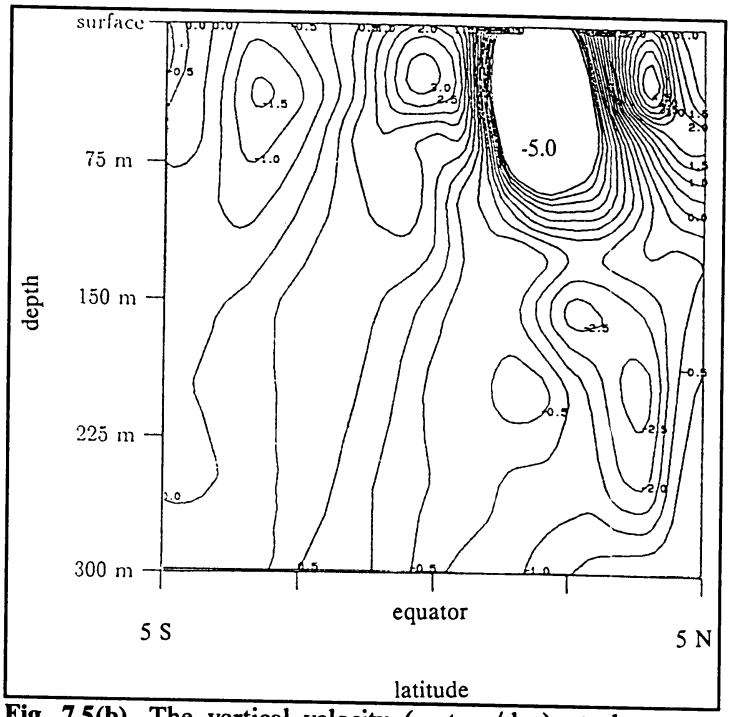

Fig. 7.5(b). The vertical velocity (meters/day) at the cross-section at 110°W.

7.4 The warm pool and the seasonal cycle

As mentioned before, surface mixing is able to deepen the western warm pool. At first the warming of the equatorial slice due to off-equatorial mixing as described in 7.1. Other mechanisms show up when we compare the two following models with one another:

1 - The PP-case (see chapter 6)

2 - The PP-case with a superficial turbulent surface layer with the depth of the Obukhov lengthscale (~ 20 m at the equator) only between 5°N and 5°S (Fig. 7.8).

In figure 7.9 the seasonal change of the region warmer than 26°C, in the equatorial slice, between 160°E and 160°W for both these cases is shown. A schematic of the equatorial zonal winds is shown in figure 7.10. The warm pool is deepest in the months December and March and shallowest in the months June and September. Figure 7.10 shows that there is only a clear seasonal cycle in the winds over the western Pacific. Comparing the case with and without a slice of surface mixing we see that the greatest difference between these two is in the months June and September when easterly winds blow over the western Pacific. We formulate the next theses:

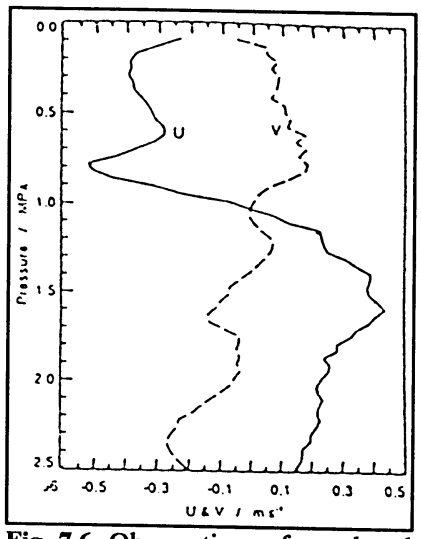

Fig. 7.6. Observations of zonal and lateral velocity (ms^{-1}) at 147°E (Brainerd and Gregg, 1991).

Theses

1. The warm pool is build up due to westerly winds in the western equatorial Pacific.
2. Surface mixing influences the position of zonal convergence in the equatorial slice. It permits a buildup of warm water when winds are easterly and it conserves an already existing warm pool.

Ad 1. Figure 7.11 shows the vertical (upward) velocity at the equator (m/day) of the PP-case (without surface mixing!) for the month December. We can divide the picture in two parts: in the western Pacific downwelling exists due to westerly winds (Fig. 7.10), in the eastern Pacific upwelling exists due to the easterly winds over the eastern Pacific. Downwelling can be associated with subsurface warming and upwelling with surface cooling. So westerly winds seem to build up the warm pool, see also Morrissey and Lander (1988).

Right at the equator the lateral component of the Coriolis force disappears, so we expect a place of convergent water motion. Due to the westerly winds which fix the position of this convergence the position of the maximal surface elevation is not at the western boundary, but at about 160°E. This could explain the counter EUC in the western Pacific.

Ad 2. Figure 7.12 shows zonal equatorial velocity fields of the two cases for the month September, when a developed warm pool only exists for the surface mixing case (Fig. 7.9(b), the right column). At the dateline at a depth of 100 m a convergence arises in the surface mixing case at the dateline where for the no surface mixing case the EUC begins to speed up at the New Guinean coast.

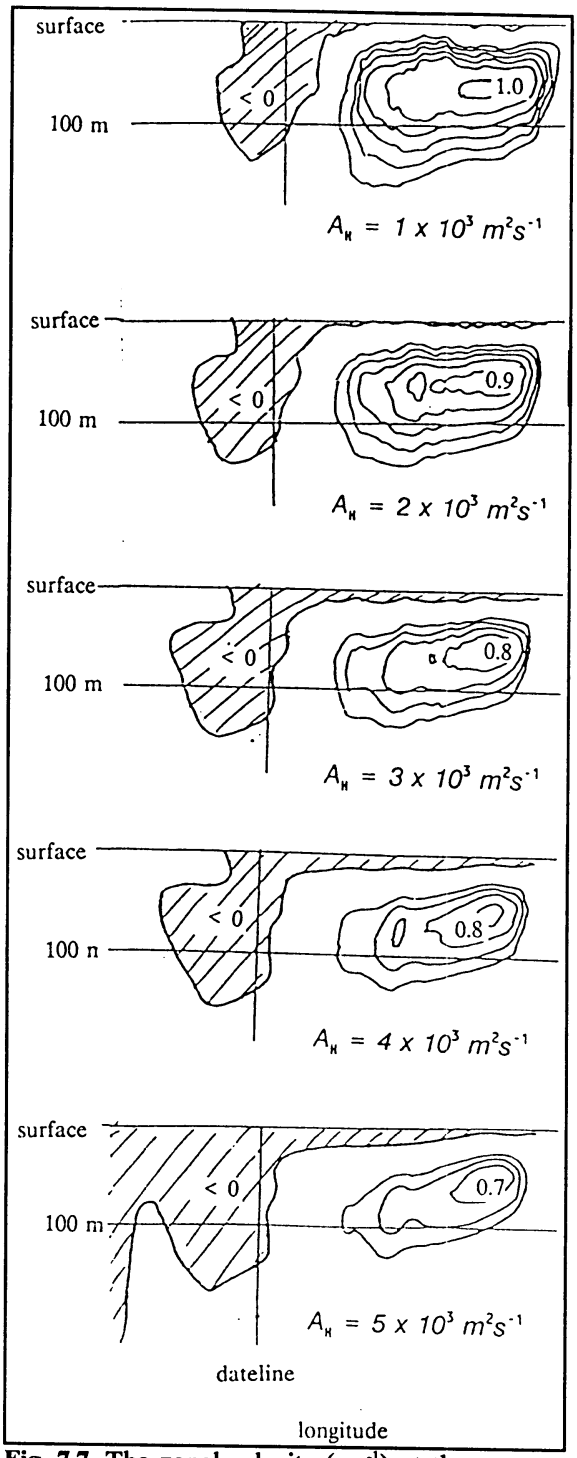

Fig. 7.7. The zonal velocity (ms^{-1}) at the equator in March for the PP-case. The horizontal diffusion is varied.

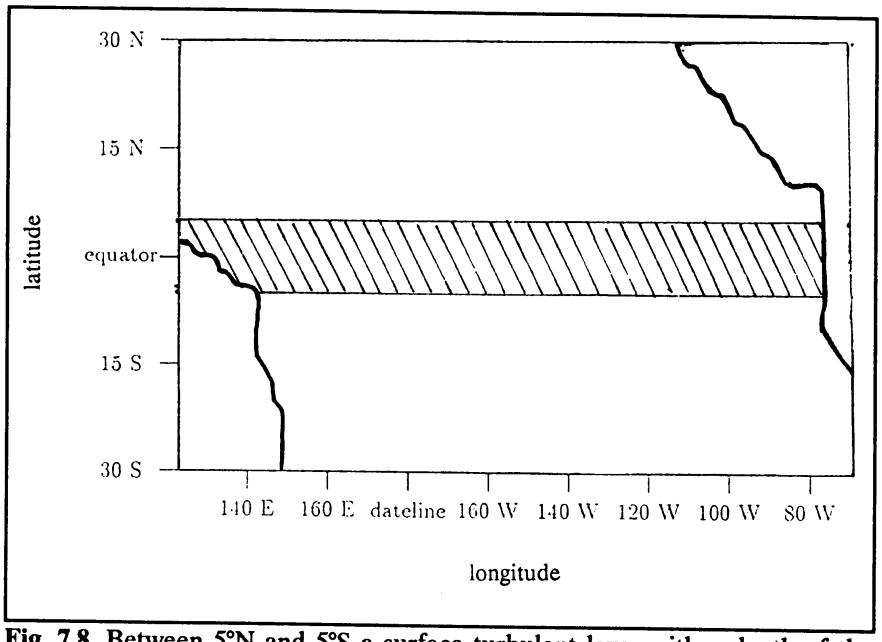

Fig. 7.8. Between 5°N and 5°S a surface turbulent layer with a depth of the Obukhov length scale is defined.

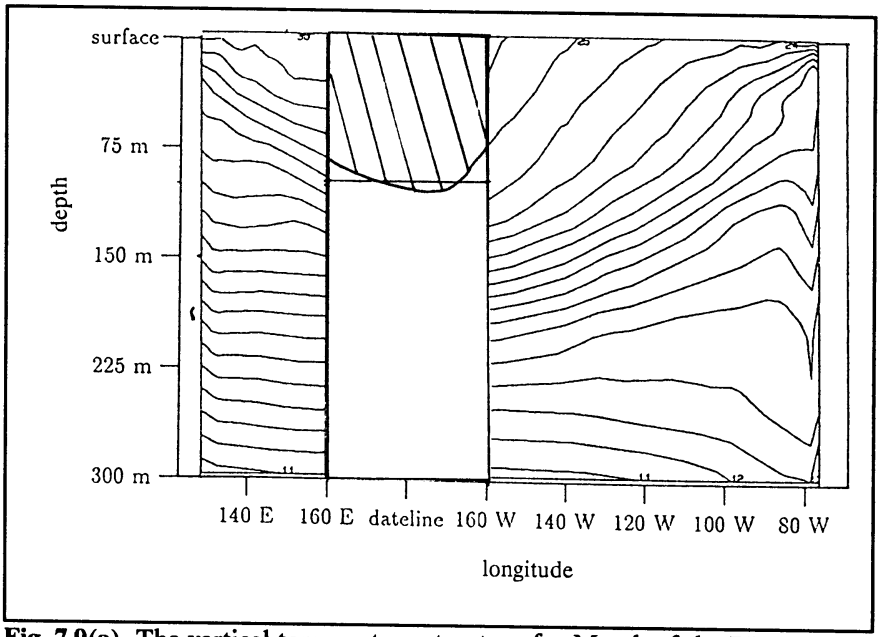

Fig. 7.9(a). The vertical temperature structure for March of the PP-case. We now consider only the 26°C between 160°E and 160°W.

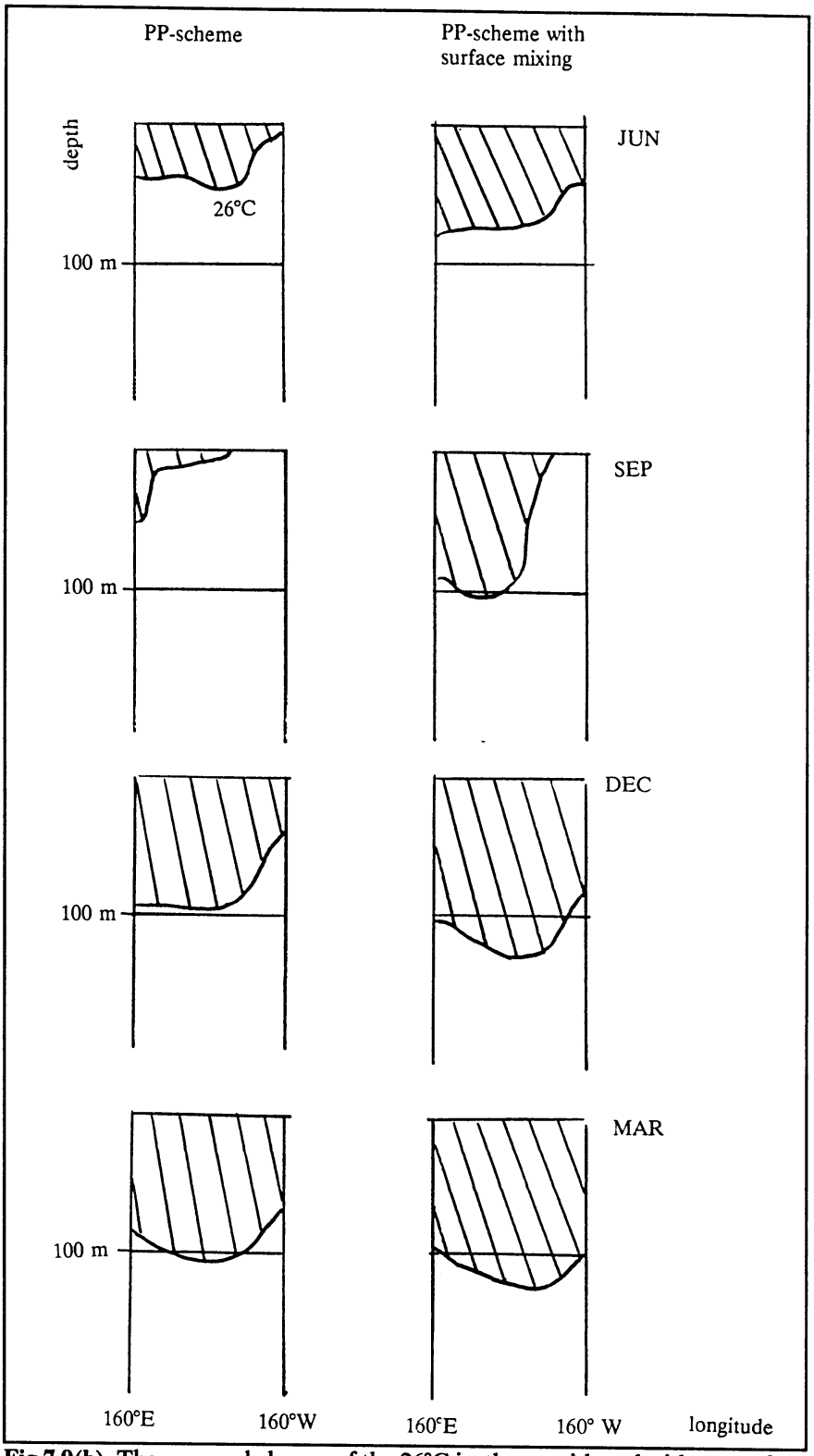

Fig 7.9(b). The seasonal change of the 26°C isotherm with and without surface mixing, 1 cm ~ 0.03 Nm^{-2}.

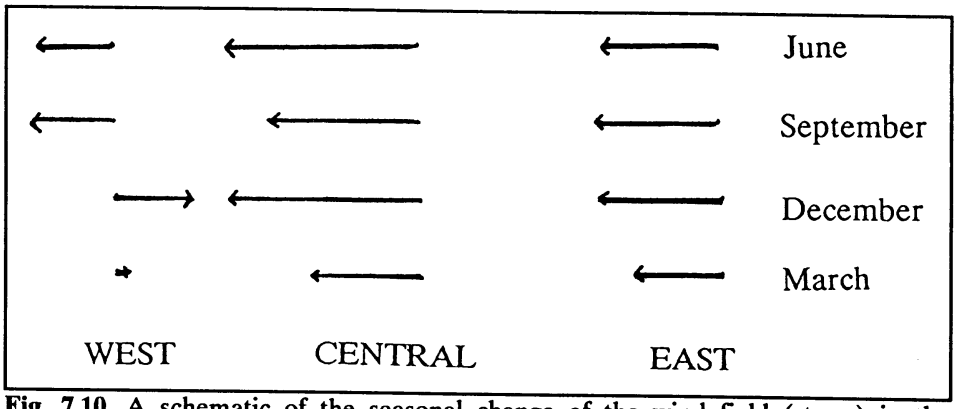

Fig. 7.10. A schematic of the seasonal change of the wind field (stress) in the western, central and eastern Pacific (1 cm ~ 0.02 Nm^{-2}).

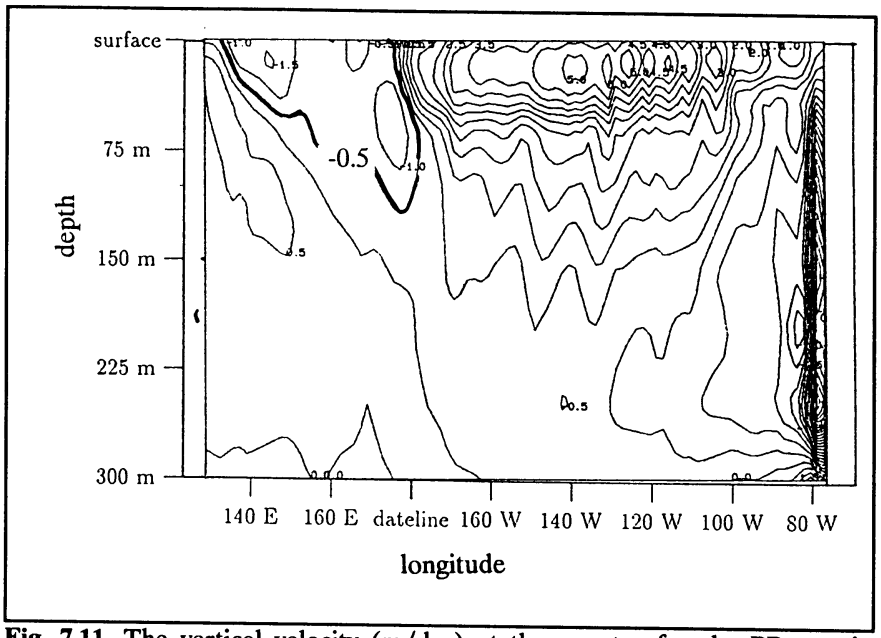

Fig. 7.11. The vertical velocity (m/day) at the equator for the PP-case in December.

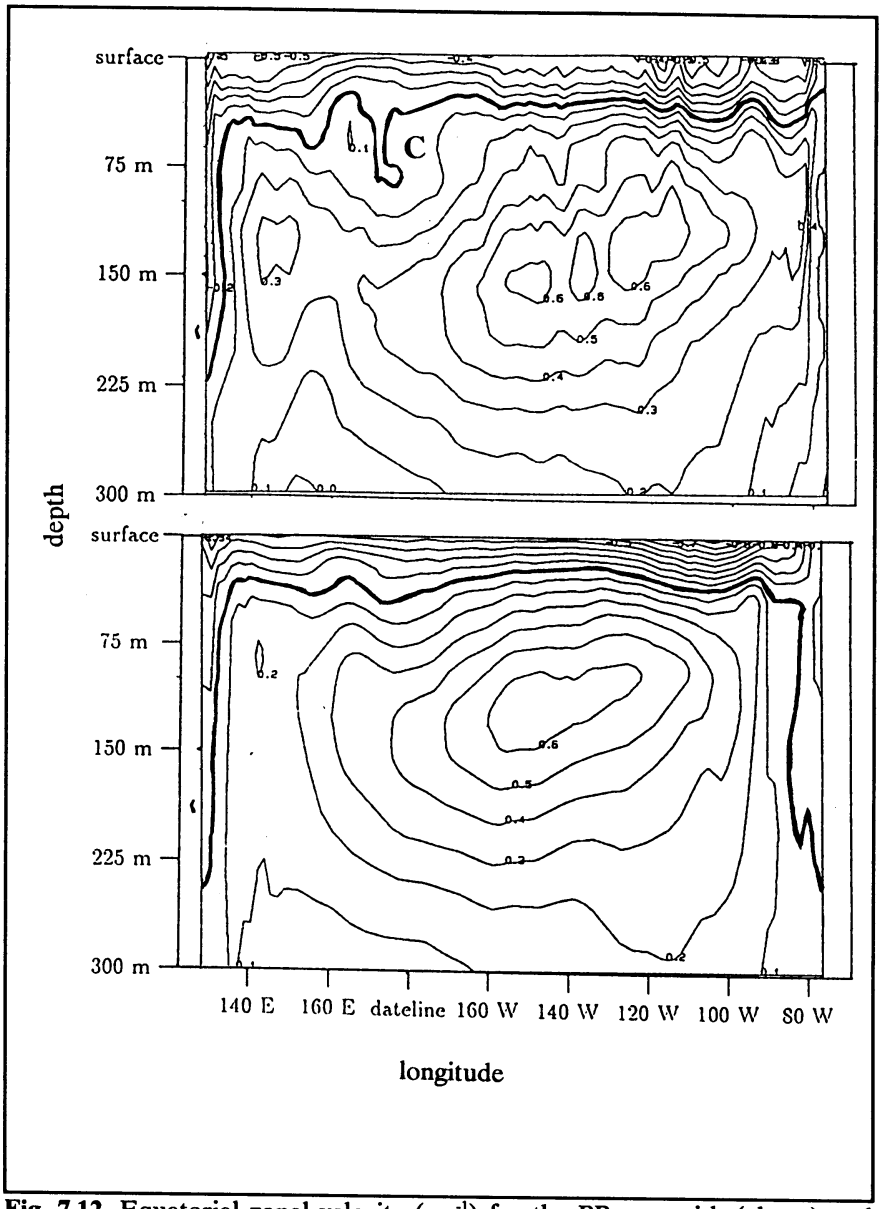

Fig. 7.12. Equatorial zonal velocity (ms^{-1}) for the PP-case with (above) and without (below) equatorial surface mixing for the month September.

8 Conclusions and future research

8.1 Conclusions

The main conclusion of this study is that in a model with relatively low resolution surface mixing causes the heat errors to decrease. The simulated SST's in the equatorial region are in better agreement with the COADS than without surface mixing. In summary

- Surface mixing improves the simulation of the equatorial SST's with respect to the data.
- Surface mixing moderates the equatorial upwelling.
- Surface mixing influences the existence and the build up of a deep warm pool
- Surface mixing changes the whole equatorial momentum balance
- Surface mixing does not improve the hot spot at 110°W, 5°N, this seems to be a resolution problem

8.2 Discussion and future research

The assumption mentioned in section 6.1 that the OGCM should produce the COADS SST's when forced with the COADS heat and salt fluxes and Hellerman and Rosenstein windstresses, is very arbitrary. Consider for example the thesis that the warm pool is build up as described in section 7.4. Westerly winds cause a build up of heat until a critical point is reached at which the warm pool "flows over", i.e. an El Niño event is initiated. In the mean annual cycle this critical point is not reached due to averaging. The mean monthly SST's however also contain El Niño event SST's. It can thus be argued that the modelled temperatures should be somewhat lower than the averaged SST's in the dataset.

Also the fact that the SST's and windfield are non-linearly coupled in reality and we're considering an uncoupled model undermines the assumption made in section 6.1. So I would suggest another experimental setup for a future model intercomparison, that may use monthly mean fluxes, but sequential and not averaged over several years.

Although improvement can be achieved by the parameterization of a surface mixed layer in an OGCM, heat errors remain too large. We believe that this is due to the too coarse resolution in the model, see also Weaver and Sarachik (1989). A higher resolution in the wind field will probably give rise to a better development of the North Equatorial Countercurrent (NECC). This may be important for the simulation of realistic SST's.

Another weak point is the parameterization of horizontal diffusion. There are indications that (counter-gradient) horizontal eddy transport is important in the equatorial region (Bryden and Brady, 1989). Maybe an eddy resolving model is needed to give a real good simulation of the equatorial dynamics.

Concluding we state that surface mixing seems to be an essential ingredient in an General Circulation Model of the tropical Pacific. We are however still far away from a truly realisic model of the equatorial Pacific!

9 References

Allaart, M.A.F. and A. Kattenberg, 1990. A primitive equation model for the Equatorial Pacific. *KNMI, Technical Report; TR-124*, De Bilt, KNMI, 41 pp.

Anderson, D.L.T. and J. Willebrand, 1992: Recent advances in modelling the ocean circulation and its effects on climate. To be published.

Batchelor, G.K., 1967: An introduction to fluid dynamics. Cambridge U.P.

Brainerd, K. and M. Gregg, 1991: Preliminary results of the COARE microstructure pilot. *TOGA Notes*, **4**, 1-4.

Bryan, K., 1991: Poleward heat transport in the ocean. *Tellus*, **43**, 104-115.

Bryden, H.L. and E.C. Brady, 1989: Eddy momentum and and heat fluxes and their effects on the circulation of the equatorial Pacific Ocean. *J. Mar. Res.*, **47**, 55-79.

Garwood, R.W.,Jr.,P.C. Gallagher, and P.Müller, 1985a: Wind direction and equilibrium mixed layer depth: General theory. *J.Phys.Oceanogr.*, **15**, 1325-1331.

Garwood, R.W.,Jr., P.Müller and P.C. Gallagher, 1985b: Wind direction and equilibrium mixed layer depth in the tropical Pacific Ocean. *J. Phys. Oceanogr.*, **15**, 1332-1338.

Gill, A.E., 1982. Atmosphere-Ocean Dynamics. New York, Academic Press, 662 pp.

Gregg, M.C., H. Peters, J.C. Wesson, N.S. Oakey and T.J. Shay, 1985: Intensive measurements of turbulence and shear in the equatorial undercurrent. *Nature*, **318**, 140-144.

Hellerman, S. and M. Rosenstein 1983: Normal monthly windstress over the world ocean with error estimates. *J. Phys. Oceanogr.*, **13**, 1093-1104.

Holton, J.R., 1979: An introduction to dynamic meteorology, Academic Press, 391 pp.

Holtslag, A.A.M., E.I.F. de Bruijn and H.-L.Pan, 1990: A high resolution air mass transformation model for short-range weather forecasting. *Mon. Wea. Rev.*, **118**, 1561-1575.

Kraus, E.B. and J.S. Turner, 1967: A one-dimensional model of the seasonal thermocline. *Tellus*, **19**, 98-106.

Latif, M., M. Flügel and J.S. Xu, 1990: An investigation of short range climate predictability in the Tropical Pacific. *J. Geoph. Res.*, **96**, 2661-2673.

Lemason, L. et B. Piton, 1968: Anomalie dynamique de la surface de la mer le long de l'equateur dans l'Ocean Pacifique. *Sér. Océanogr.*, **4**, 39-45.

Levitus, S., 1982: Climatological atlas of the world ocean. *NOAA Professional Paper*, **13**.

Morrissey, M.L. and M.A. Lander, 1988: Do equatorial westerlies precede El Niño? *Tropical ocean-atmosphere newsletter*, **46**, 1-5.

Müller, P. and R.W. Garwood Jr., 1988: Mixed layer dynamics: progress and new directions. *EOS Transactions*, **69**, 1, 2-4, 10-12.

Neelin J.D., M. Latif, M. A. F. Allaart, M.A. Cane, U. Cubasch, W.L. Gates, P.R. Gent, M. Ghil, C. Gordon, N.C. Lau, G.A. Meehl, C.R. Mechoso, J.M. Oberhuber, S.G.H. Philander, P.S. Schopf, K.R. Sperber, A. Sterl, T. Tokiaka, J. Tribbia, S.E. Zebiak, 1992: Tropical air-sea interaction in general circulation models. *Climate Dynamics*, **7**, 73-104.

Nieuwstadt, F.T.M., 1989: Turbulentie. *Dictaat, TU Delft*, 185pp.

Niiler, P.P. and E.B. Kraus, 1977: One dimensional models of the upper ocean. *Modelling and prediction of the upper layers of the ocean*, E.B. Kraus, ed., Pergamon press, 143-177.

Oberhuber, J.M., 1988: An atlas based on the 'COADS' data set: The budgets of heat, buoyancy and turbulent kinetic energy at the surface of the global ocean. Max-Planck-Institute for Meteorology / Hamburg, Report 15, 199pp.

Oberhuber, J.M., 1992: Numerical simulation of the ocean circulation. *Environmental Modelling*. P. Melli and P. Zannetti, eds., Elsevier, 287-297.

Pacanowski, R.C. and S.G.H. Philander, 1981: Parameterization of vertical mixing in numerical models of tropical oceans. *J. Phys. Oceanogr.*, **11**, 1443-1451.

Peters, H. 1990: Small-scale mixing in the Tropical Ocean. *International TOGA scientific conference proceedings / WCRP-***43**, Geneva, WMO.

Peters, H., M.C. Gregg and T.B. Sanford, 1991: Equatorial and off-equatorial fine-scale and large-scale shear variability at 140°W. *J. Geophys. Res.*, **96**, C9, 16913-16928.

Peters, H., M.C. Gregg and J.M. Toole, 1988: On the parameterization of equatorial turbulence. *J. Geoph. Res.*, **93**, C2, 1199-1218.

Philander, S.G., 1990: El Niño, La Niña and the Southern Oscillation. Academic Press. 289 pp.

Pickard, G.L. and W.J. Emery, 1990: Descriptive physical oceanography, Pergamon Press, 3rd ed., 320 pp.

Pond, S. and G.L. Pickard, 1983 Introductory dynamical oceanography, Pergamon Press, 329 pp.

Pleune, R. 1990: Vertical diffusion in the stable atmosphere. *Atmospheric Environment,* **24A**, 2547-2555.

Sarachik, E.S., 1991: Predictability of ENSO. *Climate-Ocean Interaction*, M.E. Schlessinger ed., 161-171.

Schopf, P.S. and M.E. Cane, 1983: On equatorial dynamics, mixed layer physics and sea surface temperature. *J. Phys. Oceanogr.*, **13**, 917-935.

Stull, R.B., 1988: An introduction to boundary layer meteorology, Kluwer Acad. Publ., 666 pp.

Tennekes, H and J.L. Lumley, 1972: A first course in turbulence. MIT Press.

Wacongne, S., 1989: Dynamical regimes of a fully nonlinear stratified model of the atlantic equatorial undercurrent. *J. Geophys. Res.*, **94**, C4, 4801-4815.

Weaver, A.J. and E.S. Sarachik, 1990: On the importance of vertical resolution in certain ocean general circulation models. *J. Phys. Oceanogr.*, **20**, 600-609.

Woods, J.D., 1985: The upper ocean and air-sea interaction in global climate. *The Global Climate.* J.T. Houghton, ed., Cambridge U.P., 141-187.

Yasunari, T., 1991: Monsoon and ENSO: A coupled ocean/land/atmosphere system. *TOGA Notes*, **2**, 9-13.

Appendix

Here the fields are shown of a model with between 10°N and 10°S a surface mixed layer with the G2-depth scale (Eqs. 5.9 and 5.10); outside 10°N and 10°S a layer of 50 m depth with a vertical eddy diffusivity of 10^{-3} m^2s^{-1} was defined. Below the surface layer the PP-scheme was employed (see section 4).

The last figure (Fig A.9) shows the annual mean net downward heat flux (Oberhuber, 1988)

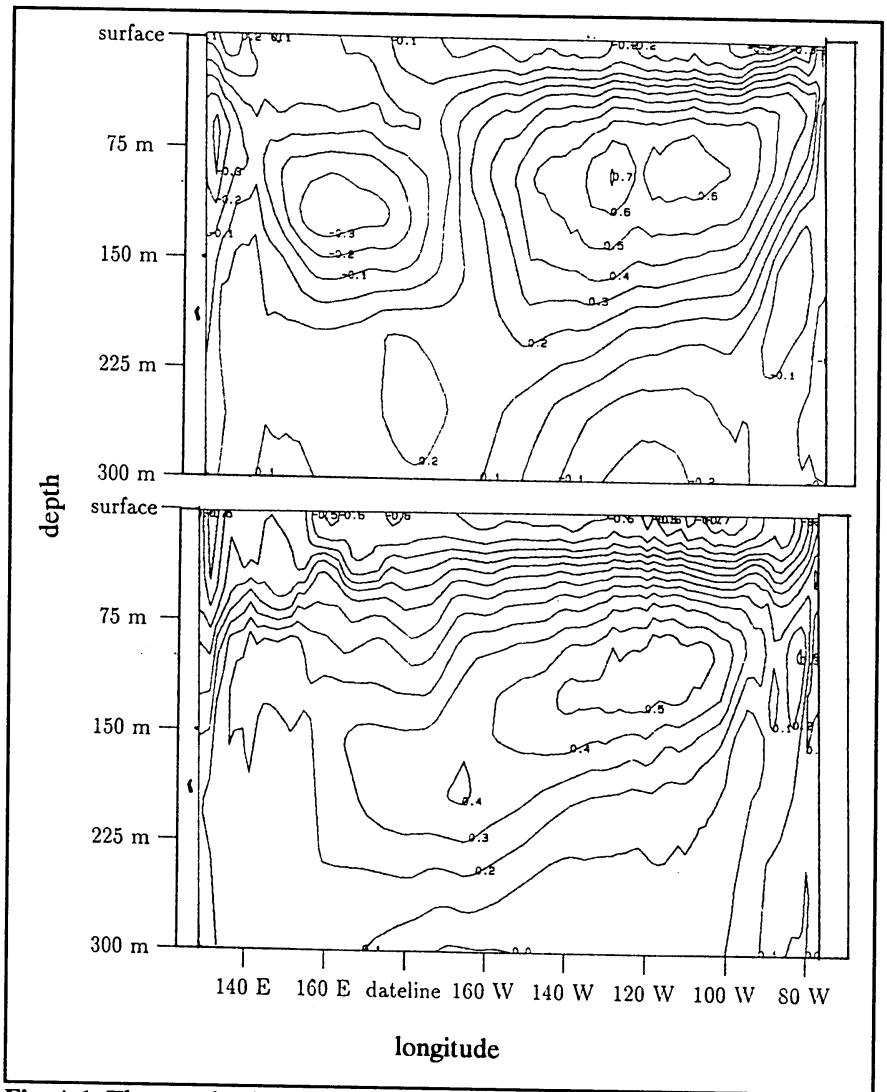

Fig. A.1. The zonal velocity in March (above) and June (below), contours are 1.0 ms^{-1}. Note the counter EUC in March.

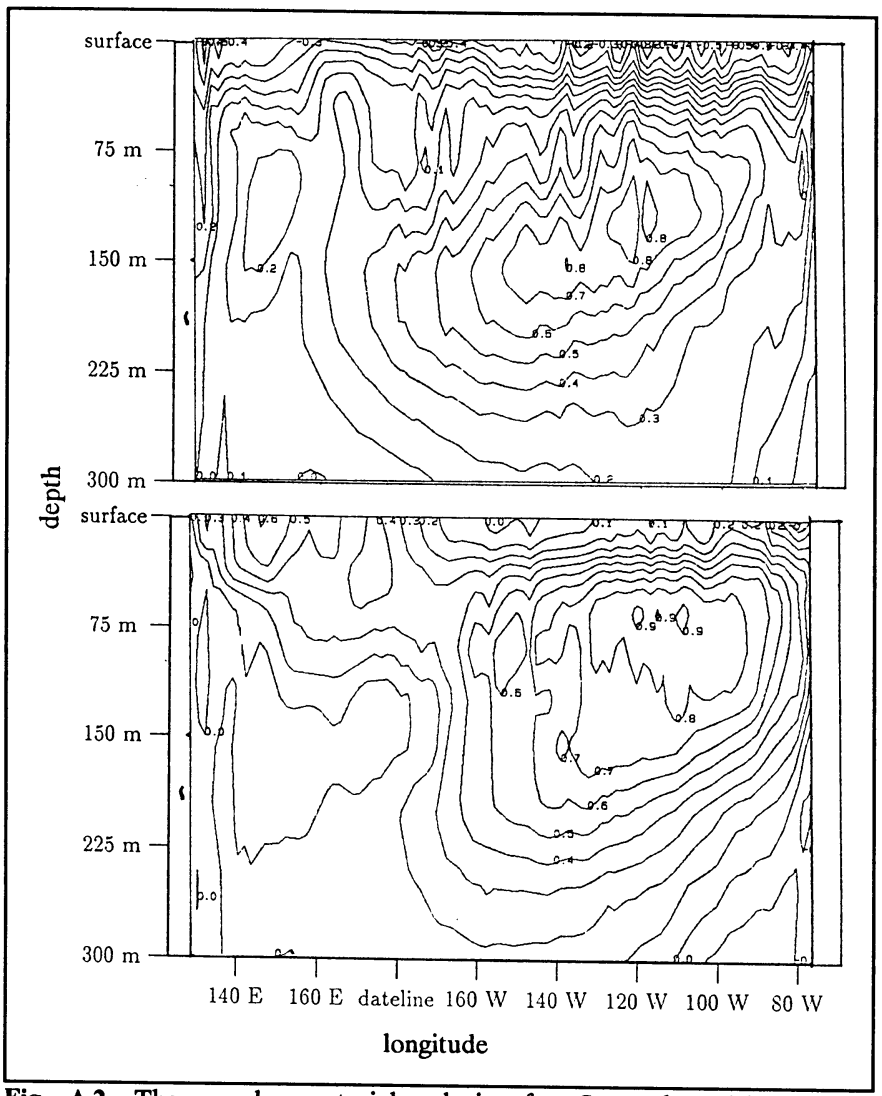

Fig. A.2. The zonal equatorial velocity for September (above) and December(below). The contours are 1.0 ms^{-1}.

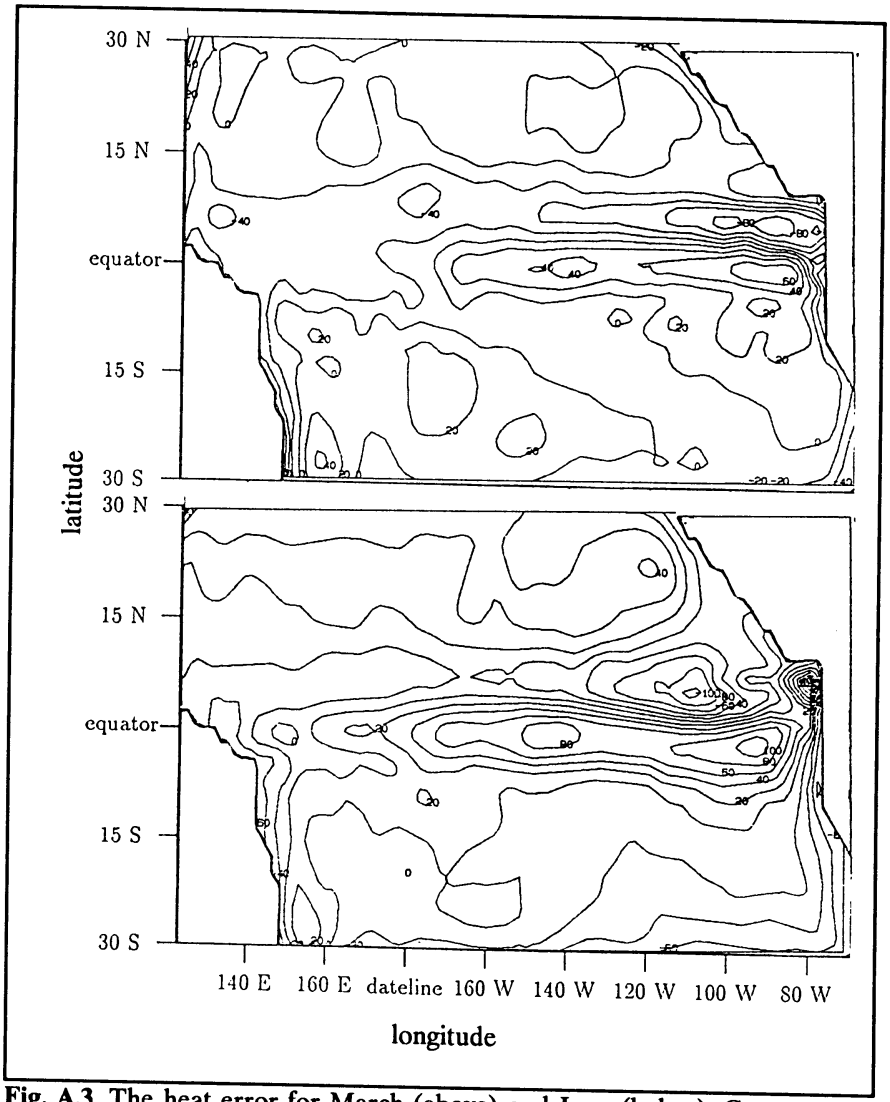

Fig. A.3. The heat error for March (above) and June (below). Contours are $20Wm^{-2}$.

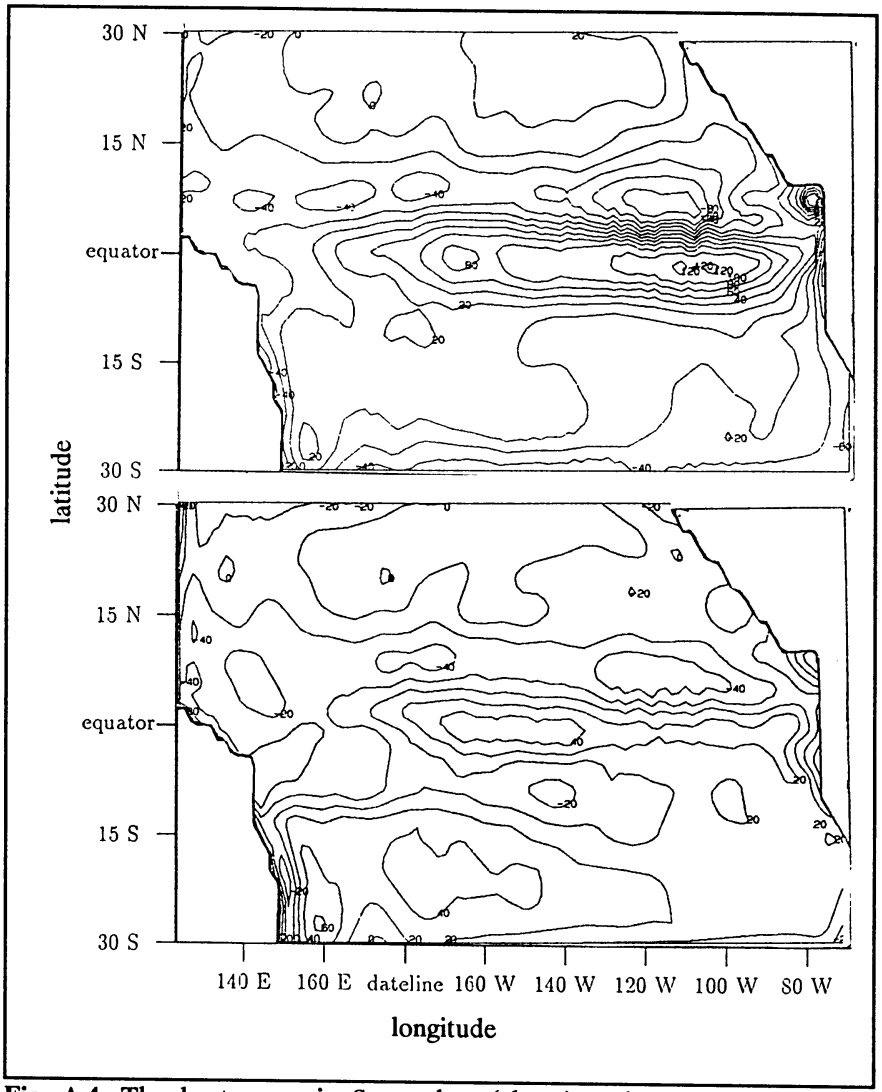

Fig. A.4. The heat error in September (above) and December (below). Contours are 20 Wm^{-2}.

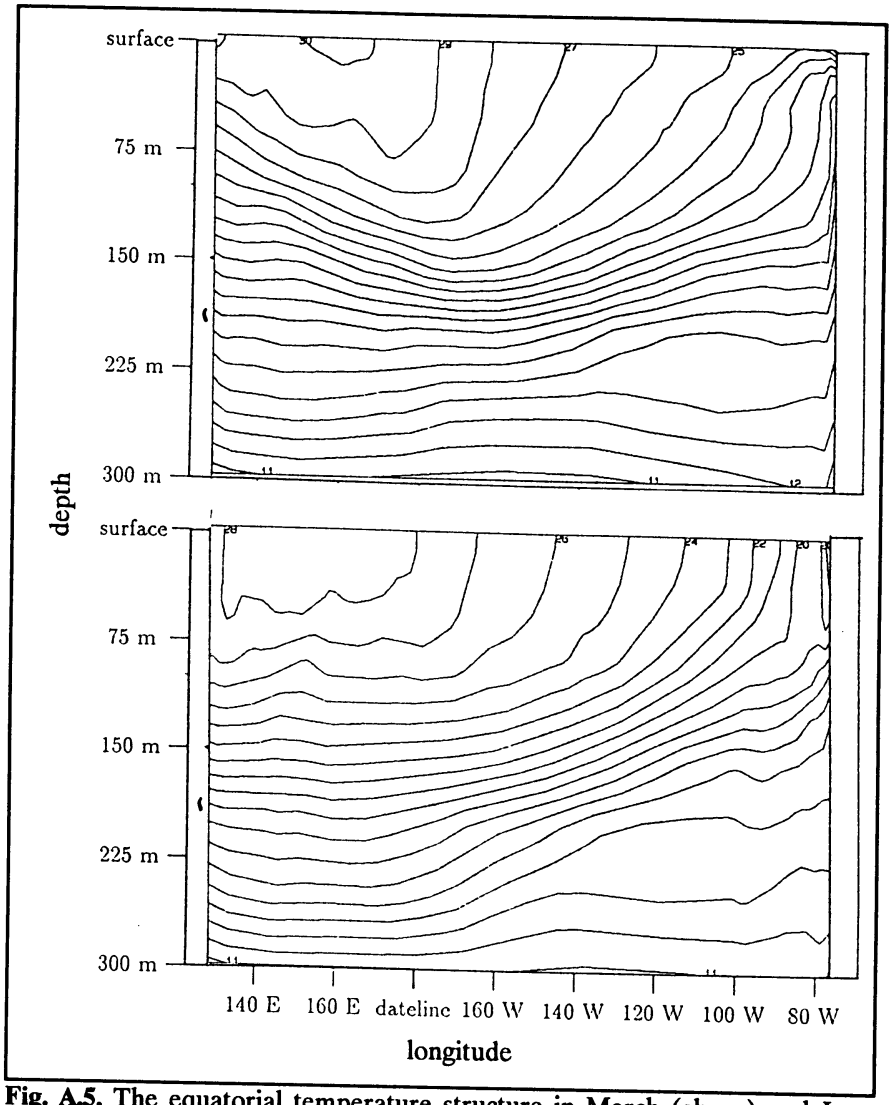

Fig. A.5. The equatorial temperature structure in March (above) and June (below). Contours are 1.0 °C.

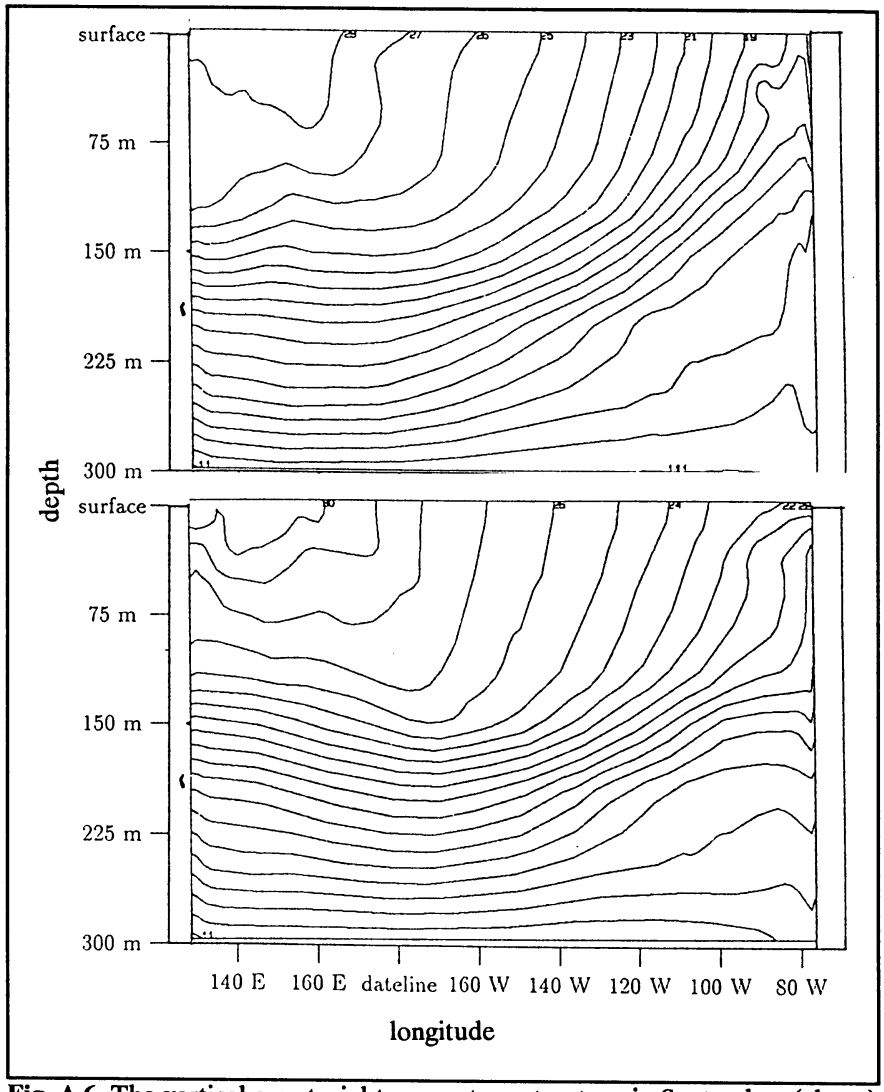

Fig. A.6. The vertical equatorial temperature structure in September (above) and December (below), contours are 1°C.

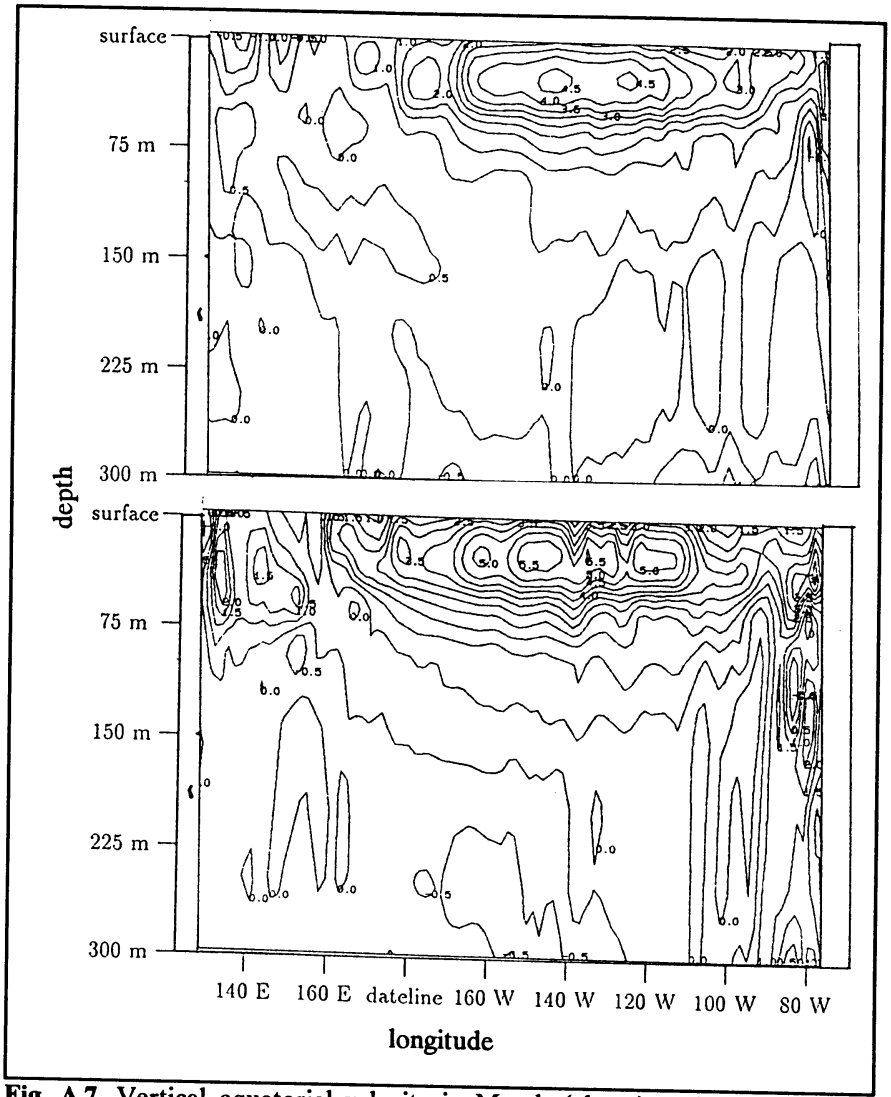

Fig. A.7. Vertical equatorial velocity in March (above) and June (below). Contours are 1.0 m/day.

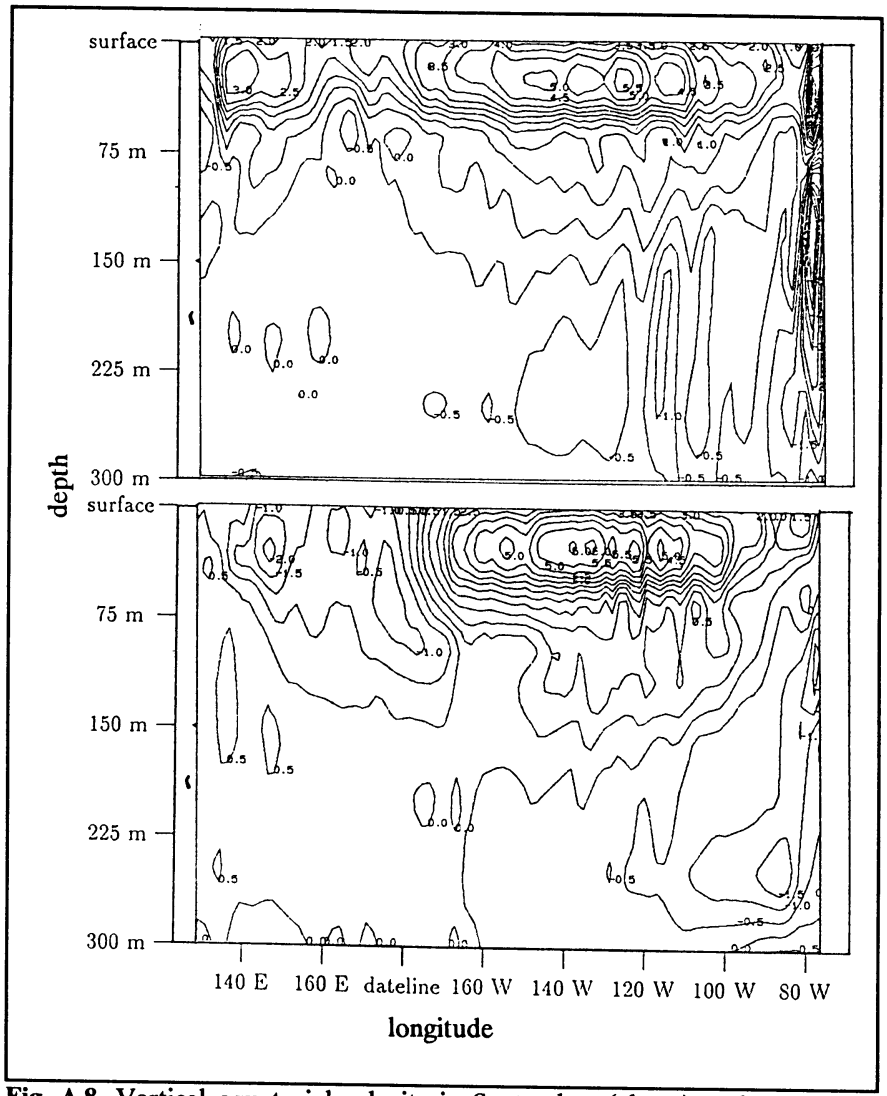

Fig. A.8. Vertical equatorial velocity in September (above) and December (below). Contours are 1.0 m/day.

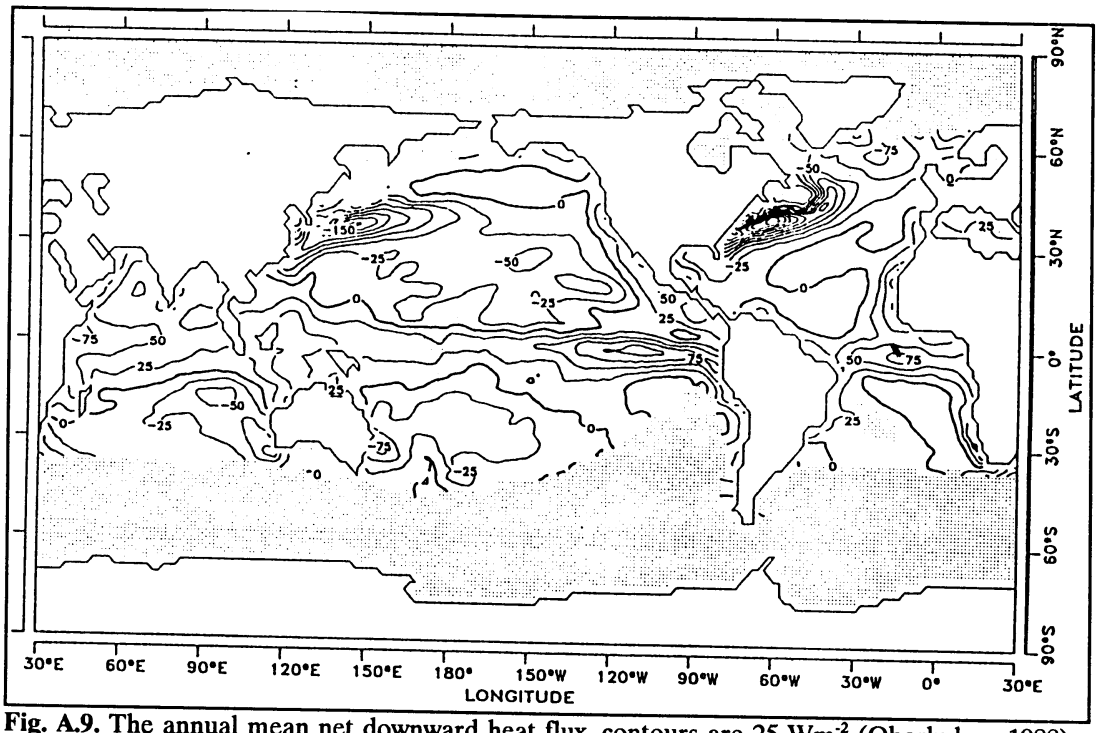

Fig. A.9. The annual mean net downward heat flux, contours are 25 Wm^{-2} (Oberhuber, 1988).